Modeling of Core Properties of Ultralight Sandwich Plates

by

Dirk Mohr

Diplom-Ingenieur, University of Karlsruhe (1999)

Submitted to the Department of Civil and Environmental Engineering
in partial fulfillment of the requirements for the degree of

Master of Science

at the

MASSACHUSETTS INSTITUTE OF TECHNOLOGY

May 2000

Author .....
Department of Civil and Environmental Engineering
May 5, 2000

Certified by .....
Tomasz Wierzbicki
Professor of Applied Mechanics
Thesis Supervisor

Certified by .....
Shi-Chang Wooh
Associate Professor of Civil and Environmental Engineering
Thesis Reader

Accepted by .....
Daniele Veneziano
Chairman, Department Committee on Graduate Students

Modeling of Core Properties of Ultralight Sandwich Plates

by

Dirk Mohr

Submitted to the Department of Civil and Environmental Engineering
on May 5, 2000, in partial fulfillment of the
requirements for the degree of
Master of Science

Abstract

An analysis of the three-dimensional macroscopic mechanical properties of metallic honeycomb is performed using a mix of analytical and numerical methods. This work demonstrates that it is feasible to use highly complex micromechanical analysis to determine the macroscopic core properties of an ultralight sandwich plate. The results describe the elastic and the inelastic behavior of the core of a commercially available honeycomb sandwich plate under uniaxial stress states.

All analysis are carried out for quasi-static loading. A representative elementary volume or a full-size model of the microstructure of honeycomb is analyzed according to the macroscopic property to be determined. Depending on the microstructural failure mode, numerical simulations are either performed with the explicit finite element code LS-DYNA or the implicit code ADINA. Analytical models are introduced to complete and verify the numerical results. The results are presented by macroscopic stress-strain curves as well as by macroscopic stress-volumetric strain curves.

Thesis Supervisor: Tomasz Wierzbicki
Title: Professor of Applied Mechanics

Acknowledgments

I owe a great deal of gratitude to Professor Tomasz Wierzbicki who gave me the opportunity to engage in research on crashworthiness.

I am also indebted to the *Studienstiftung des deutschen Volkes* for partially sponsoring my studies at MIT.

Thanks to Professor Shi-Chang Wooh for his valuable support.

Finally, I wish to thank my colleagues at the Impact and Crashworthiness Laboratory and my office mates for their support.

Contents

List of Figures

Chapter 1

Introduction

The objective of the present study is the modeling of the core properties of ultralight sandwich plates. Ultralight sandwich plates certainly have the potential to revolutionize the car industry in the next decade. By using aluminium sandwich panels in a modern car body, weight reductions of up to 50% can be expected. In addition to that, honeycomb sandwich plates show optimal sound and thermal insulation properties. Santosa [9] showed in his thesis the superb crashworthiness performance of thin-walled members reinforced with an ultralight metal core.

To optimize sandwich panels for the use in car bodies, reliable modeling techniques must be available. In the automotive industry, commercial finite element codes like LS-DYNA, ADINA, ABAQUS or PAM-Crash are commonly used to simulate the mechanical behaviour of a car body. LS-DYNA as well as PAM-Crash provide a material model for metallic honeycomb. These models describe the cellular material honeycomb macroscopically as a three-dimensional continuum. Thus, both programs require input curves that relate all six components of the macroscopic stress tensor to the corresponding compenents of the stress tensor or to the volumetric strain (respectively).

The present study determines the macroscopic mechanical properties of metallic honeycomb for large macroscopic strains and distorsions. Analytical as well as numerical methods are used for this task. Since the explicit finite element code LS-DYNA will be used for the analysis of the microstructure of the honeycomb, the second chapter discusses some important aspects of the numerical modeling with LS-DYNA. In addition to that, one macroscopic material model for honeycomb in LS-DYNA is briefly presented.

The third chapter and the appendix show the micromechanical analysis and the resulting macroscopic description in detail. A short discussion of the macroscopic material properties and concluding remarks are given in chapter 4.

Chapter 2

Numerical Modeling with LS-DYNA

2.1 Quasi-static Modeling with explicit time integration

2.1.1 Problem statement

Most simulations presented within this thesis are performed with the explict version of the finite element code LS-DYNA. Thus, a well-known problem of the modeling of quasi-static tests with explicit codes arises: The total CPU-time for a simulation is becoming extremely lengthy.

In contrast to implicit codes, LS-DYNA restricts the maximum time step size. A discussion of the numerical stability of the explicit time integration scheme [1] shows that this critical time step Δt_{crit} is proportional to the square root of the characteristic mass m of the problem:

$$\Delta t_{crit} \propto \sqrt{m} \tag{2.1}$$

The the total duration t_{crush} of the crushing of the specimen is inversely proportional to the characteristic velocity v of the problem:

$$t_{crush} \propto \frac{1}{v} \tag{2.2}$$

Based on the assumption, that the total CPU-time is proportional to the number of time steps Δt_{crit} necessary to obtain the solution over the time interval $[0..t_{crush}]$, the following statement can be made:

$$t_{CPU} \propto \frac{1}{v\sqrt{m}} \tag{2.3}$$

In order to reduce the total time of the computation, LS-DYNA offers the option to add artificial mass by increasing the material density. Its efficiency with respect to the total CPU time can be directly seen from equation (2.3).

Obviously, this option violates the physical formulation of the problem and can yield wrong and non physical results. This is an issue in any transient analysis using mass scaling. Especially in quasi-static simulations, it can have a strong impact on the results. In the ideal case, the attribution of inertia effects to the solution, charcterized by the kinetic energy E_{kin} should completely disappear:

$$v \to 0 \qquad \text{and thus:} \qquad E_{kin} \to 0 \tag{2.4}$$

The numerical analysis with an explicit code would be impossible. Therefore, a weak formulation of (2.4) can be made by comparing the kinetic to the internal energy E_{int}:

$$\frac{E_{kin}}{E_{int}} \ll 1 \tag{2.5}$$

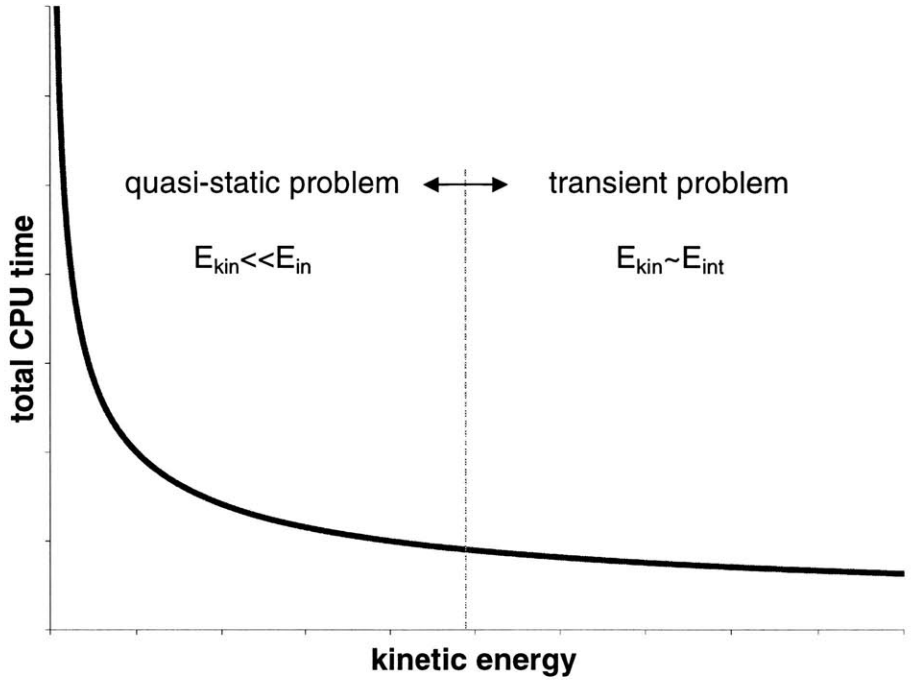

Figure 2-1: Conflict of total CPU time and kinetic energy in explicit FEM codes

The order of magnitude of the kinetic energy is proportional to the product of the square of the characteristic velocity and the characteristic mass:

$$E_{kin} \propto mv^2 \tag{2.6}$$

Combining equations (2.3) and (2.6), a very simple expression describing the relationship between the total CPU time and the kinetic energy can be derived:

$$t_{CPU} \propto \frac{1}{\sqrt{E_{kin}}} \tag{2.7}$$

2.1.2 Problem treatment

The conflict of holding the quasi-static assumption and working with reasonable CPU-times is treated the following way: The charcteristic velocity was fixed at the beginning of the simulation.

In most cases an arbitrary value $v = 1000mm/s$ was chosen. Starting with the true physical density of the material, the mass was highly scaled (up to plus 1000 %) by the activated mass scaling option in LS-DYNA. In a second step, the ratio of kinetic over internal energy was surveyed throughout the whole simulation. The assumption (2.5) was translated into finite values by chosing:

$$\frac{E_{kin}}{E_{int}} \leq 10^{-2} \tag{2.8}$$

Meeting this assumption (2.8) is very difficult; especially at the beginning of the simulation. In order to improve the quality of the solution in this phase, a sinusodial velocity profile was used. It must be noted however, that the latter method was only applied to simulations that required a high quality of the solution in the initial phase of the simulation.

2.2 Reduced-Integrated Belytschko-Lin-Tsay Shell Element

2.2.1 Element Formulation

The default shell element formulation in LS-DYNA3D follows the formulation developed by Belytschko, Lin and Tsay. This bilinear four-node quadrilateral shell element uses a one-point integration scheme in combination with an hourglass control algorithm.

The formulation of this element is clearly optimized towards a computationally efficient algorithm. Thus the element includes lots of simplifications that reduce the number of operations per time step and element dramatically.

The element formulation is based on the Mindlin theory of plates and shells. In addition to that a corotational coordinate system is introduced. The velocities of the midsurface and the angular velocities of the cross-section are bilinearly interpolated over the element. A corotational coordinate system follows the material during deformations. This basically yields linear and frame-invariant kinematic and kinetic relations. The corotational velocity-strain formulation precludes the use of large time steps, but this is no drawback in an explicit time integration code like LS-DYNA, where the numerical stability usually limits the time steps to a magnitude where errors in the integration of the rate formulation are negligible.

2.2.2 Hourglass Control

To discuss hourglassing, the shape functions $h_i, i = 1..4$ are expressed by base functions of the corresponding polynomial space. The base functions for Q_1 elements are $1, s, t, st$. The vector of

the shape functions $\boldsymbol{h}$ is a linear combination of these base functions:

$$4\boldsymbol{h} = \boldsymbol{\Sigma} + \boldsymbol{\Lambda}_1 s + \boldsymbol{\Lambda}_2 t + \boldsymbol{\Gamma} st \tag{2.9}$$

with

$$\boldsymbol{h}^T = \left\{ \begin{array}{cccc} h_1 & h_2 & h_3 & h_4 \end{array} \right\} \tag{2.10}$$

$$\boldsymbol{\Sigma}^T = \left\{ \begin{array}{cccc} 1 & 1 & 1 & 1 \end{array} \right\} \tag{2.11}$$

$$\boldsymbol{\Lambda}_1^T = \left\{ \begin{array}{cccc} -1 & 1 & 1 & -1 \end{array} \right\} \tag{2.12}$$

$$\boldsymbol{\Lambda}_2^T = \left\{ \begin{array}{cccc} -1 & -1 & 1 & 1 \end{array} \right\} \tag{2.13}$$

$$\boldsymbol{\Gamma}^T = \left\{ \begin{array}{cccc} 1 & -1 & 1 & -1 \end{array} \right\} \tag{2.14}$$

If the shape functions h_i are used to interpolate elemental midsurface displacements or cross-section rotations, equations (2.10)-(2.14) can be interpreted physically. The vector $\boldsymbol{\Sigma}$ represents the rigid body mode corresponding to the degree of freedom that is interpolated; the vectors $\boldsymbol{\Lambda}_i, i = 1, 2$ represent regular displacement modes. Since the one-point integration neglects the nonlinear portion of the displacement field, it is the vector $\boldsymbol{\Gamma}$ that includes the hourglass mode. Illustrations of these four modes can be found in [2].

The reduced integrated Belytschko-Lin-Tsay(BLT) shell interpolates the fields that correspond to its five nodal degrees of freedom with the shape functions introduced above; thus, the reduced-integrated BLT-element contains five zero-energy patterns [5]. For simplicity, only one degree of freedom will be considered in the following.

To correct the finite element solution from these hourglassing deformations, anti-hourglass forces are added to the nodes. In a first step, the current velocity field is decomposed into a linear portion and the hourglass velocity field:

$$\dot{\boldsymbol{u}} = \dot{\boldsymbol{u}}^{LIN} + \dot{\boldsymbol{u}}^{HG} \tag{2.15}$$

The vector $\boldsymbol{u}$ represents the four nodal velocities. It is shown in [2] that the hourglass field is orthogonal to the linear and constant displacement field; the nodal hourglassing velocities can be expressed by the hourglass mode vector $\boldsymbol{\Gamma}$ and a modal hourglassing velocity $\dot{q}$:

$$\dot{\boldsymbol{u}}^{HG} = \dot{q}\boldsymbol{\Gamma} \tag{2.16}$$

In addition to the hourglass modal vector, the hourglass shape vector $\boldsymbol{\gamma}$ is introduced:

$$\dot{q} = \frac{1}{\sqrt{8}} \dot{\boldsymbol{u}} \boldsymbol{\gamma} \tag{2.17}$$

The hourglass shape vector relates the hourglass modal velocities to the nodal velocities $\dot{\boldsymbol{u}}$. This expression is very powerful: by using the orthogonality of the shape function base vectors the hourglass shape vector can be computed directly from the hourglass base vectors and the B-Matrix of the current configuration.

Additionally, the hourglass shape vector is orthogonal to the linear velocity field. It determines the direction and the distribution of the artificial nodal forces $\boldsymbol{f}^{HG}$ that are applied to correct the occurring zero-energy modes.

$$\boldsymbol{f}^{HG} = Q\boldsymbol{\gamma} \tag{2.18}$$

This hourglass modal velocity is used to compute the intensity Q of the artificial nodal forces. Two methods are implemented into LS-DYNA. The first approach is to apply artificial damping to the hourglass modes:

$$Q = 2\epsilon\omega_{max}\left(\frac{\rho V}{8}\right)\dot{q} \tag{2.19}$$

The major shortcoming of the hourglass damping approach is that, mesh distortion - included in the displacement field - is permanent. This method allows hourglassing, but prevents the mesh from violent oscillations.

The second approach, is the use of an artificial stiffness:

$$Q = \kappa K_{max} q \tag{2.20}$$

The hourglass coefficients ϵ and κ are used to control the artificial damping or the artificial stiffness (respectively). Following Flanangan and Belytschko [2], the use of artificial stiffness is more successful. Both methods are offered in LS-DYNA; although they could be combined, they can only be applied separately.

2.3 Artificial Bulk Viscosity

Bulk viscosity is used to treat shock waves. In the presence of shocks, the governing partial differential equations can give multiple weak solutions. Unmodified finite element equations often will not produce even approximately correct answers for such problems. The adding of artificial bulk viscosity smoothens shock waves and eliminates the solution space from discontinuities - the new problem possesses a unique solution. The influence of the bulk viscosity is assumed to be insignificant outside the shock layer and thus, shock problems can be modeled with a finite element code.

The bulk viscosity formulation in LS-DYNA uses the volumetric strain rate $\dot{\epsilon}_v$ to evaluate the artificial viscosity term q that is added to the physical pressure [4]:

$$q = \rho l(C_0 l\dot{\epsilon}_v^2 + C_1 c\dot{\epsilon}_v) \qquad \text{if} \qquad \dot{\epsilon}_v > 0 \tag{2.21}$$

$$q = 0 \qquad \text{if} \qquad \dot{\epsilon}_v < 0 \tag{2.22}$$

with

$$\dot{\epsilon}_v = -(\dot{\epsilon}_{11} + \dot{\epsilon}_{22} + \dot{\epsilon}_{33}) \tag{2.23}$$

where l is a characteristic element length, ρ the density and c the sound speed. C_0 and C_1 are dimensionless constants that can be adjusted by the user. Their default is 1.5 and .06 respectively.

The concept of artificial bulk viscosity origins from compressible fluid dynamics where large rates-of-change of the element's volume occur in shock wave problems only. Usually, when modeling solid metallic structures under dynamic loading, bulk viscosity enters the elastic behaviour but certainly does not influence the plastic response since the incompressibility must be guaranteed.

For metallic honeycomb, the presence of artificial bulk viscosity influences the analysis with LS-DYNA. As shown in chapter 4, deformations of metallic honeycombs are accompanied by a change of the material density. Consequently, the bulk viscosity term enters the solution even if there is no shock wave to be modeled [10].

To assure that the quasi-static analysis are free from artificial viscosity, both constants C_0 and C_1 must be set to zero.

2.4 Material Model 26: Metallic Honeycomb

The material model 26 in LS-DYNA originates in the modeling of deformable barriers made out of hoenycomb. Material model 26 is an orthotropic material model that defines its material properties in a local material coordinate system. The elastic properties vary linearly between the properties of the uncompressed honeycomb and the fully compressed honeycomb. The internal variable describing this non-linear elasticity is the volumetric strain ϵ_v:

$$\begin{Bmatrix} \sigma_{11} \\ \sigma_{22} \\ \sigma_{33} \\ \tau_{12} \\ \tau_{13} \\ \tau_{23} \end{Bmatrix} = \underbrace{\begin{pmatrix} E_{11} & 0 & 0 & 0 & 0 & 0 \\ 0 & E_{22} & 0 & 0 & 0 & 0 \\ 0 & 0 & E_{33} & 0 & 0 & 0 \\ 0 & 0 & 0 & G_{12} & 0 & 0 \\ 0 & 0 & 0 & 0 & G_{13} & 0 \\ 0 & 0 & 0 & 0 & 0 & G_{23} \end{pmatrix}}_{\boldsymbol{C}(\beta)} \begin{Bmatrix} \epsilon_{11} \\ \epsilon_{22} \\ \epsilon_{33} \\ \gamma_{12} \\ \gamma_{13} \\ \gamma_{23} \end{Bmatrix} \tag{2.24}$$

with

$$\boldsymbol{C}(\beta) = \boldsymbol{C}_0 + \beta(\boldsymbol{C}_s - \boldsymbol{C}_0) \qquad \text{and} \qquad \beta = max\left\{min\left(\frac{\epsilon_v^{max}}{\epsilon_v}, 1\right), 0\right\} \tag{2.25}$$

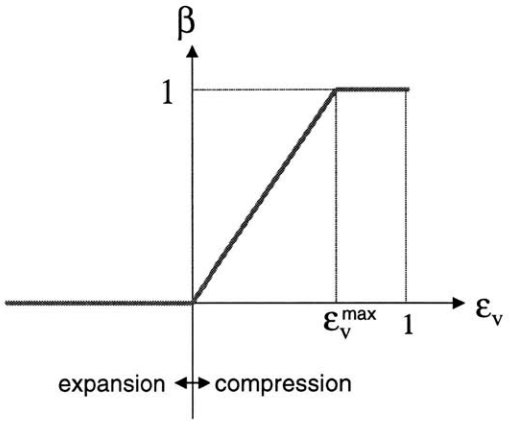

Figure 2-2: Elastic hardening coefficient as fonction of the volumetric strain

where $\boldsymbol{C}$ is a diagonal material matrix that describes the elastic properties of the honeycomb. $\boldsymbol{C}_0$ contains the elastic properties of the uncompressed honeycomb; $\boldsymbol{C}_s$ represents the elastic properties of the fully compacted honeycomb and therefore corresponds to the stiffness matrix of the solid cell wall material with terms on the diagonal only. The plastic behavior of the metallic honeycomb is modeled by simple hardening plasticity model. A yield surface is defined as a function of the volumetric strain. Corresponding to each component of the stress vector, a load curve must be given. Each of these six curves describes the stress as function of the volumetric strain.

Chapter 3

Experimental Crushing of a Honeycomb-Sandwich Plate

3.1 Specimen

Only one type of a double walled sandwich is tested experimentally. The specimen consists of a double walled sandwich with a honeycomb core. It is manufactured by Alusuisse and has the following characteristics:

- top face: AlMg1 (AA5005A) H22 plate; thickness $t_t = 0.5mm$, yield stress $\sigma_0 = 80MPa$;
- bottom face: same material as top face, thickness $t_b = 1mm$;
- core: height $C = 5mm$, honeycomb, aluminium alloy (solid material properties not known); axial crushing strength $\sigma_f = 2MPa$; measured geometry[1]: $t = 0.1 \div 0.3mm$, $h \approx 4.0mm$, $l \approx 3.2mm$, $\theta \approx 28°$ (see Fig. 4-1 for the definition of the geometric variables);
- sandwich specimen: quadratic specimen were cut from a large sandwich plate; the size of each specimen is $50mm \times 50mm$;

Due to manufacturing, the geometry deviates from the ideal configuration that is later assumed in the theoretical and numerical evaluations. Five double walled sandwich samples and three samples without top plate are crushed.

3.2 Testing Procedure

The specimens are axially crushed on a MTS testing machine with a capacity of 90 kN. They are placed between two flat parallel metallic surfaces. The testing characteristics are the following:

- crushing speed: 0.1 mm/s
- reading frequency: 100 Hz
- maximum crushing length: 3.9 mm

3.3 Interpretation of the testing results

The five tests of the double-walled sandwich show the same stress-displacement evolution (Fig. 3-2). The stresses are defined as the crushing force per sample area - here $A = 2500mm^2$. The same

[1]The measurements were not exact; on one hand, the thickness of the cell wall varies a lot as can be seen through a magnifying glass; on the other hand, the surface was partly covered by the adhesive that glues the cover surfaces of the honeycomb

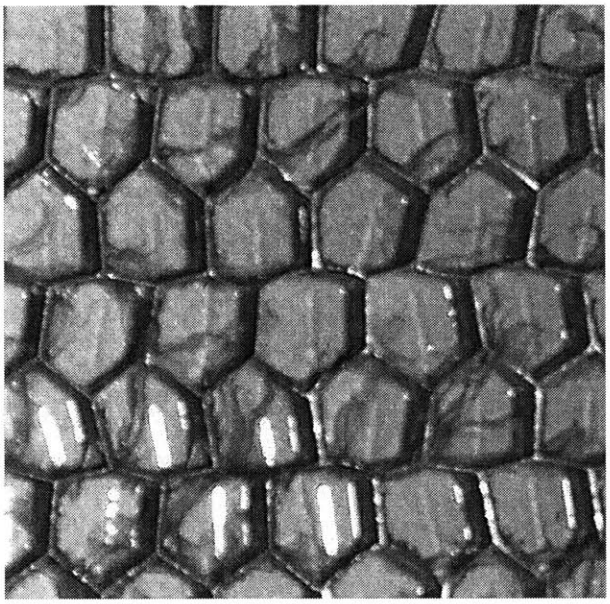

Figure 3-1: Single-walled specimen

is valid for the test series without top plate (Fig. 3-3). However, the crushing force-displacement diagram for this sandwich element is different from the well reported crushing of honeycomb without top and bottom plates (fig. 3-4).

For a very long honeycomb cells the crushing force-displacement diagramm shows a high initial peak and then oscillates around a much lower mean crushing force (fig. 3-4). The number of oscillations corresponds to the number of folds created during the axial crushing. The half wave length H of these folds is a pure geometric variable and is independent from the material properties. It depends on the cell wall thickness t and the cell geometry (characteristic width D) [11]:

$$H = 0.821\sqrt[3]{tD^2} \tag{3.1}$$

The crushing force of the double-walled specimen is strongly dominated by the interface between the cell walls and the solid outer layers. Applying equation (3.1) to the geometric data of a specimen the half wave length for a honeycomb core with free boundaries (no top or bottom plate) is expected to be in the order of magnitude of $1mm$. The height of the honeycomb core is therfore small compared to the length of one fold; the single-walled specimen with the free boundaries on the top shows one fold before the glued boundary dominates the crushing force curve. The half wave length can be measured in figure 3-3. The measured value of $H = 0.8mm$ is close to the analytical estimation made

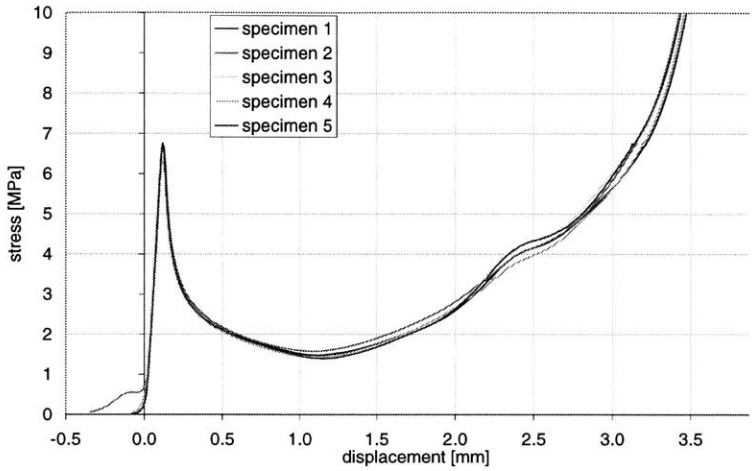

Figure 3-2: double-walled sandwich: axial compression stress over displacement

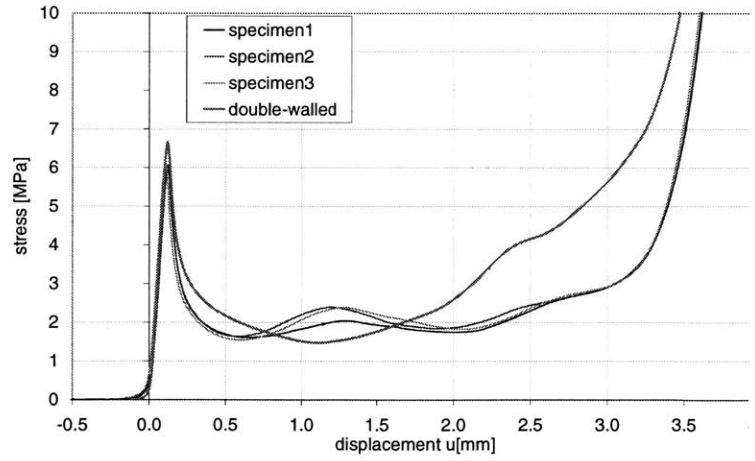

Figure 3-3: single-walled sandwich: axial compression stress over displacement

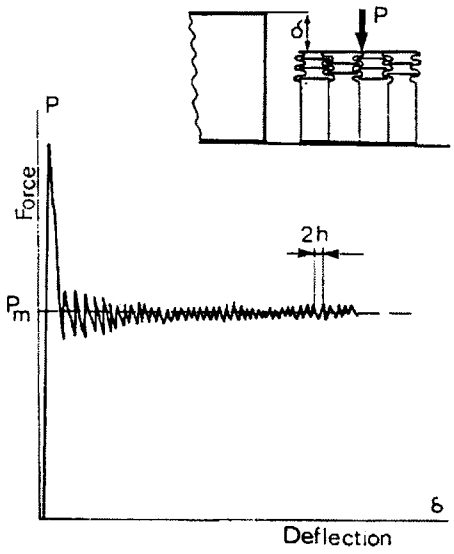

Figure 3-4: Typical crushing force-deflection curve for honeycomb without top/bottom plate

before. The inverse analysis of that geometric problem delivers for the experimentally determined half wave length and the measured D a cell wall thickness of $t \approx 0.1mm$. This corresponds very well to the cell wall thicknesses that were previously obtained from measurements.

The amplitude of the initial peak basically depends on the imperfections of the undeformed microstructure. Following the analytical analysis of Wierzbicki [11], the mean crushing force of an elementary cell is a function of the yield stress and the plastic hardening of the solid cell wall material:

$$P_m = 8.61\sigma_m t^{\frac{5}{3}} D^{\frac{1}{3}} \qquad \text{with} \qquad \sigma_m = f(\sigma_0, hardening) \tag{3.2}$$

where σ_m denotes an average flow stress that is higher than the initial yield stress σ_0. Using a mean crushing stress of $2MPa$ as it is given by Alusuisse, an inverse analysis yields to a mean stress acting in the cell wall of $\sigma_m \approx 105MPa$. In the further analysis the yield stress of the solid aluminium is assumed to $\sigma_0^s = 100MPa$ and a isotropic hardening modulus of $E_T^s = \frac{E}{700} = 100MPa$ [2].

The following chapter on the numerical and analytical evaluation of the macroscopic properties of honeycomb uses the cell wall material and geometric properties that were determined before as

[2]These values result from a brief parameter study of the corresponding numerical model, that will be presented in chaper 4. Numerical analysises with different values for σ_0^s and E_T^s were performed. The analysis with $\sigma_0^s = 100MPa$ and $E_T^s = 100MPa$ showed the best agreement with the experimental crushing force evolution

input data. It must be noted, that the analysis in chapter 4 primarily focusses on the method of how to determine the macroscopic material properties and the qualitative discussion of the macroscopic core behavior. Therefore, the input data that has been determined in this chapter deals only as an example for the cell wall properties of the core of an commercially available sandwich panel. The out-of-plane crushing of a sandwich plate and the interpretation of the experimental results is used to give a first approximation of the microstructural properties.

Chapter 4

Numerical and analytical evaluation of the macroscopic properties of honeycomb

This chapter discusses the mechanical behavior of the cellular material honeycomb. In contrast to many solid materials, the microstructure of honeycomb is highly visible and can be appreciated without magnification. The microstructure is made of thin walls that form a hexagonal cell. These elementary cells or elementary columns are aligned in an array and thus build the honeycomb microstructure.

The micromechanical analysis leads to a better understanding of the macroscopic behaviour of the structure. The aim of this chapter is the use of reliable techniques to find the macroscopic material properties of metallic honeycomb. This requires a mix of analytical and numerical evaluations. It must be noted, that all macroscopic stresses and strains that are used in this thesis are defined with respect to the current configuration of the honeycomb.

4.1 Geometry of a honeycomb cell

The characteristic honeycombed cross-section has two orthotropy axes. All cell walls that are situated in the (x_2, x_3)-plane have a double thickness due to the manufacturing process. Most metallic honeycombs are made by expanding strip-glued sheds. As result, each hexagonal cell has four walls of thickness t and two walls of thickness 2t. The colored triangle in figure 4-1 highlights the elementary cross-section area of the honeycomb. Gibson *et al.*[3] give the relationship for the area of this triangle:

$$A_{\triangle} = (h + sin\theta l)\, cos\theta l \tag{4.1}$$

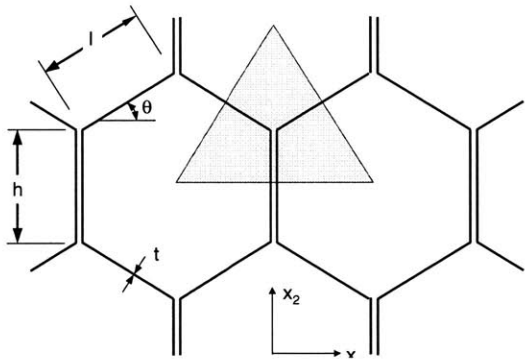

Figure 4-1: Honeycomb cell geometry

and thus, for a strip-glued honeycomb the area ratio:

$$\frac{A_s}{A^*} = \frac{\frac{h}{l} + 1}{\left(\frac{h}{l} + sin\theta\right) cos\theta} \frac{t}{l} \tag{4.2}$$

where A^* denotes the macroscopic area of the honeycomb and A_s the effective area of the solid material.

4.2 Crushing in x_3-direction

4.2.1 Young's Modulus

The Young's modulus is obtained by applying the theory of mixtures. Thus, the volume ratio $\frac{A}{A^*}$ relates the macroscopic elastic property E_3^* of the metallic honeycomb to the Young's modulus E_s of the solid aluminium:

$$E_3^* = \frac{A}{A^*} E_s \tag{4.3}$$

4.2.2 Compression

To evaluate the macroscopic properties in x_3-direction, a representative elementary volume (Y-model, see figure A-2) with the corresponding symmetry boundary conditions is studied [6]. As shown by Wierzbicki [11] and Seggewiss [6], the failure of the adhesive between two neighboring cell walls must be considered in order to predict the axial mean crushing force correctly. This requirement will not be fullfilled within this thesis. Instead of two cell walls that are glued with an adhesive, a monolithic cell wall with doubled thickness will be considered. This means that this study only includes folding mechanisms with a firm joint between two neighboring cells.

The result of a numerical simulation of the single-walled sandwich (no top plate) is shown in figure

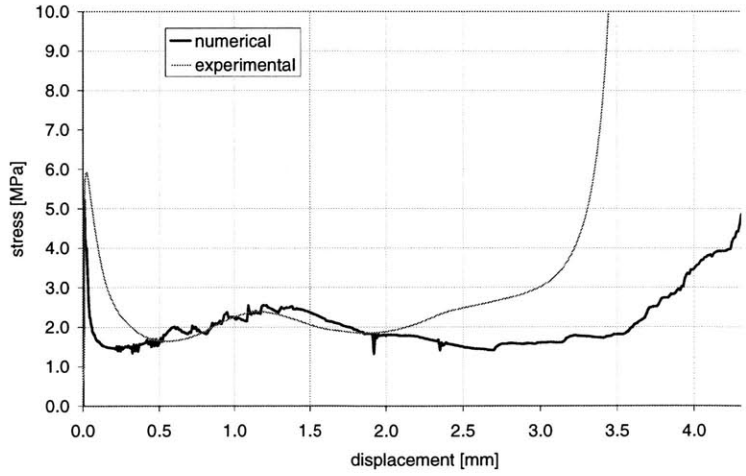

Figure 4-2: Single-walled sandwich: Comparison of numerical(firm joints) and experimental results

4-2. Detailed information about the numerical model and plots of the deformed mesh can be found in appendix A.1. The mean crushing stress of 2 MPa is approximately met by this numerical simulation. However, the drop of the initial peak force as well as the densification phase are poorly approximated. The densification starts later in the numerical analysis than in the experiments. In addition to the kinematic restriction to folding mechanisms with firm joints, there are several sources for the deviation of the numerical response:

- Glue on the cell walls: The glue used to connect the honeycomb with the outer layers (top and bottom plates) covers the complete plate surface with a thin layer. In addition to that, this glue enters the honeycomb cells and covers the cell walls as well. Thus, the physical shell wall contact thicknesses are bigger than assumed in the finite element analysis.
- Modeling of the cell wall corners: The geometric interpolation of the cell wall corners with 4-node finite-elements is very crude. The contact algoritm cannot detect penetrations in the corners. Therefore, the cell walls are closer in the numerical model than in reality.
- Fracture: It can be seen from the specimen that the aluminium locally fractures in highly tensioned areas. This can be seen from the finite element analysis as well; the principal strains in some elements (especially in cell wall corners) increase up to 100%. Although the fractures in the microstructure do not cause any discontinuities in the macroscopic stress-strain curve, the presence of local fractures certainly incluences the macroscopic response. Since the fracture is not included in the numerical model, deviations of the numerical response due to missing fracture must be expected;
- Interface top plate-honeycomb: The honeycomb core and the outer layers are connected with glue. In the numerical analysis, the glue is assumed to be rigid; thus, the glue could be replaced by boundary conditions, that set all degrees of freedom at the interface surface to zero;

4.2.3 Tension

The inelastic mechanical properties for axial tension are evaluated analytically analogous to the evaluation of the macroscopic Young's modulus. This analysis yields the very simple formulas for the yield stress $\sigma^*_{3,0}$ and the tangent modulus $E^*_{3,T}$:

$$\sigma^*_{3,0} = \frac{A}{A^*}\sigma^s_0 \qquad \text{and} \qquad E^*_{3,T} = \frac{A}{A^*}E^s_T \tag{4.4}$$

4.2.4 Transformation from the Macroscopic Strains ϵ_{33} to Volumetric Strains

The material model 26 in LS-DYNA (see 2.4) requires the input data as a function of the volumetric strain ϵ_v. Thus, the macroscopic stress-strain curve that was evaluated previously must be transformed into a macroscopic stress-volumetric strain curve. Poisson's effects are neglected in the case of compression or tension in the x_3-direction. Consequently, this transformation is trivial:

$$\epsilon_v = -\epsilon_{33} \tag{4.5}$$

4.3 Crushing in x_2-direction

4.3.1 Young's Modulus E_2^*

The macroscopic Young's modulus E_2^* is proportional to the bending stiffness of the thin cell walls. In a first approximation, the cell-walls in the (x_2, x_3)-plane do not influence the macroscopic stiffness in x_2-direction. Thus, the evaluation of the bending stiffness gives:

$$E_2^* = \left(\frac{t}{l}\right)^3 \frac{h/l + sin\theta_0}{cos^3\theta_0} E_s \tag{4.6}$$

4.3.2 Compression

Under compression the microstructure is expected to collapse and form an irregular, non-symmetric deformation pattern. Thus, the inelastic properties are evaluated numerically. Papka *et al.* [7] simulated the transverse crushing of honeycomb by the use of two different numerical models:

1. Representative microstructure: Only one closed cell and its neightboring cell walls are considered.
2. Full scale analysis: The numerical model represents the whole geometry of an experimental specimen, e.g. 9×6 cells;

Their research demonstrates that the plateau-regime is only poorly approximated by the first model. Therefore, within this thesis a full scale analysis of a cross-section is performed. Artificial imperfections are not introduced into the initial geaometry of the finite element mesh; however, the quasi static loading provokes elastic waves that correspond to small initial displacement patterns simulating an imperfect structure. Plots of the cross-section and its distinct states of deformation can be found in appendix A.2. Figure 4-3 shows the macroscopic stress-strain for the crushing in x_2-direction.

The honeycomb collapses at approximately $0.06MPa$. Figures A-10 to A-13 show, that both uncollapsed and collapsed configurations coexist at the same macroscopic stress level. The model captures very well the characteristic localization of the crushing. It can be seen from figures A-14 to A-16 that collapse propagates in the microstructure and brings about small oscillations around a mean crushing stress until densification due to contacting cell walls occurs and thus stiffens the microstructure.

4.3.3 Tension

Under tension, a regular deformation pattern is expected. Gibson *et al.* give the exact plastic collapse load by analyzing a single cell. As for the Young's modulus, the double-thickness walls do not contribute to the plastic collapse load since the failure mode is dominated by the bending of the thin cell walls:

$$\sigma^*_{2,pl} = \left(\frac{t}{l}\right)^2 \frac{\sigma^s_0}{2cos^2\theta} \tag{4.7}$$

Equation (4.7) was derived for a ideally plastic material with the yield stress σ^s_0. Since hardening of the solid material goes with the plastic deformation of the microstructure, a numerical simulation with the implicit finite element code ADINA is performed. Figure 4-5 shows the two curves describing the evolution of the macroscopic stress σ_{22} when tension is applied. For large macroscopic strains (e.g. $\epsilon_{22} > 10\%$), the influence of the hardening becomes significant for the macroscopic material properties.

4.3.4 Kinematics and Transformation to Volumetric Strains

The relationship between the macroscopic strain ϵ_{22} and the volumetric strain ϵ_v can be directly evaluated from the y-displacement measured in the numerical experiment. The volumetric strain ϵ_v is obtained by analyzing a kinematically representative part of the cross-section (see figure 4-6). In the idealized model, the in-plane displacement depends on the angle θ only. When the angle becomes zero, the width B of the representative cross-section remains constant ($B = l$) and the evolution of the volumetric strain is proportional to the macroscopic strain ϵ_{22}:

$$\epsilon_v = 1 - \frac{1+\epsilon_{22}}{cos\theta_0} cos\left\{arcsin\left[\left(\frac{h}{l} + sin\theta_0\right)(1+\epsilon_{22}) - \frac{h}{l}\right]\right\}, \qquad \theta > 0 \tag{4.8}$$

$$\epsilon_v = 1 - \frac{1+\epsilon_{22}}{cos\theta_0}, \qquad \theta = 0 \tag{4.9}$$

The same kinematic mode that is shown in figure 4-6 for the compression of the honeycomb is assumed for the kinematics if tension is applied. Equation (4.8), is valid for $\theta < \theta_0$ (compression) as well as for $\theta_0 < \theta < \theta_{max}$ (tension), where θ_{max} denotes the angle when the cell walls get into contact and densification begins. Equation (4.8) is plotted in figure 4-7. The curve shows, that the relationship between the macroscopic strain ϵ_{22} and the volumetric strain is not strongly monotonous. Since the material model 26 requires only one function for the stress in x_2-direction (over the volumetric strain) and as a consequence of the lacking monotony, material model 26 in LS-DYNA is unable to represent a different behaviour for tension and compression in x_2-direction.

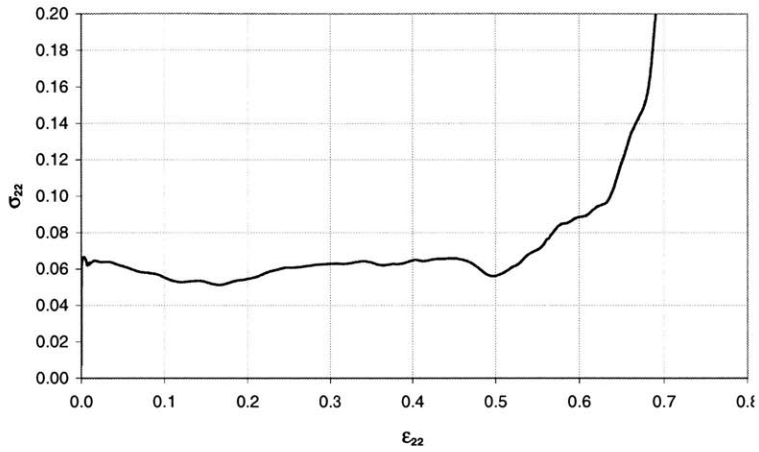

Figure 4-3: Macroscopic stress-strain curve for compressive crushing in x_2-direction

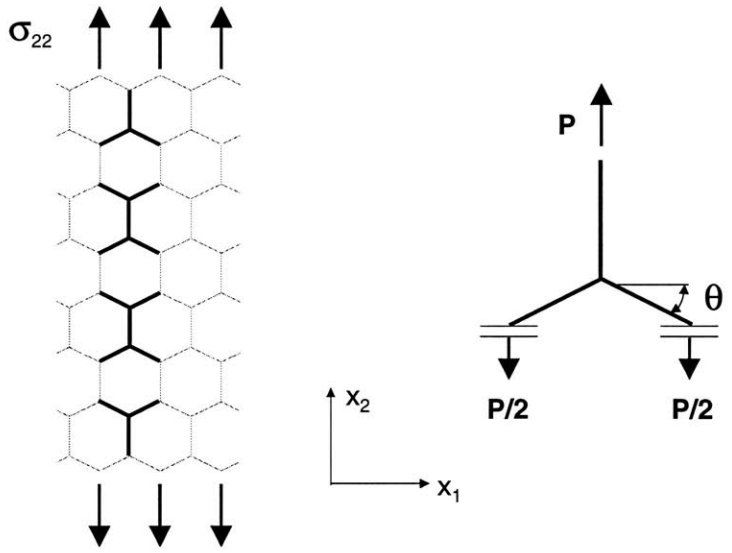

Figure 4-4: Representative microstructure for tension in x_2-direction

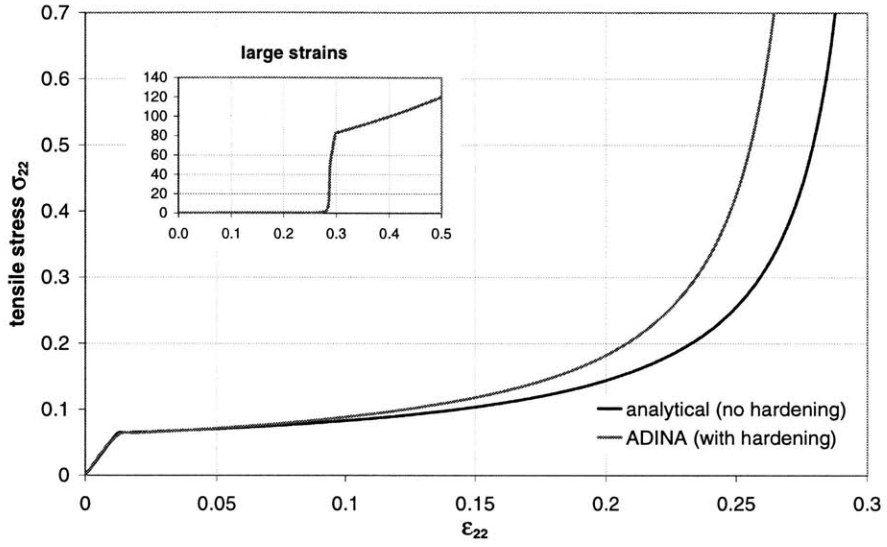

Figure 4-5: Macroscopic stress-strain curve for tension in x_2-direction

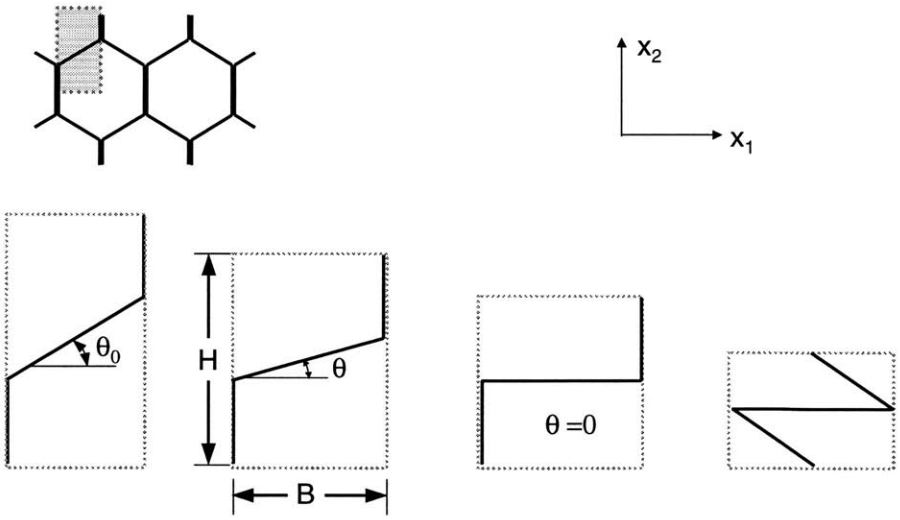

Figure 4-6: Simplified kinematics of the crushing in x_2-direction

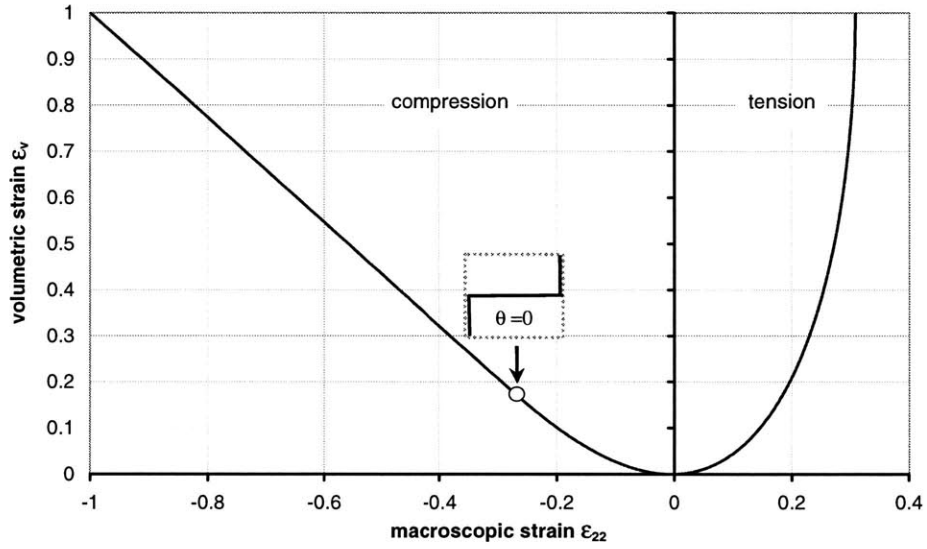

Figure 4-7: Relationship between the volumetric strain ϵ_v and the macroscopic strain ϵ_{22}

4.4 Crushing in x_1-direction

4.4.1 Young's modulus

Since all double-thickness cell walls are perpendicular to the macroscopic material axis to be analyzed the macroscopic material properties are is not influenced by these walls. The uniaxial loading by bands of the thin cell walls (fig. 4-8). Their elementary mechanical sytem is a clamped beam. Thus, the Young's modulus E_1^* is given by the bending stiffness that beam:

$$E_1^* = \left(\frac{t}{l}\right)^3 \frac{cos\theta}{(h/l + sin\theta)sin^2\theta} E_s \tag{4.10}$$

Using this formula, a Young's modulus of $E_1^* = 5MPa$ is found for the given honeycomb.

4.4.2 Tension

The same mechanical system as introduced for the evaluation of the Young's modulus is used (fig. 4-8). Considering bending only, Gibson *et al.* [3] derived the plastic collapse load for an ideally plastic material:

$$\sigma_{1,pl}^* = \left(\frac{t}{l}\right)^2 \frac{\sigma_0}{2(h/l + sin\theta)sin\theta} \tag{4.11}$$

Expression (4.11) neglects the influence of the normal force in the elementary beam and assumes two plastic hinges at both clamped ends. This expression can be used as a first approximation for large rotations around the plastic hinges, too. The corresponding macroscopic stress-strain curve is plotted in figure 4-9. The sigularity at $\epsilon_{11} = 0.13$ is due to the $sin\theta$-term in the denominator, that disappears since θ approaches zero.

To obtain more detailed information about the mechanical behaviour for macroscopic strains greater than $\epsilon_{11} > 0.1$, an analysis for large deformation of the elementary beam is performed with the implicit finite element code ADINA. The result is traced in figure 4-9. The behaviour of the microstructure can be characterized by three distinct plastic phases. The first phase is bending dominated meaning that the internal energy of that system is highly localized in the two plastic hinges. In a transistion phase, the nature of the system changes dramatically. The lever of the force P gets very small as well as the displacement in x_1-direction that is associated to a rotation increment $\Delta\theta$. Thus, the microstructure stiffens geometrically until the stresses due to the normal force reach the yield stress and the crushing enters a third phase that is characterized by a macroscopic hardening. In contrast to the two preceeding phases where the macroscopic hardening was due to a changing geometry, the macroscopic hardening in the third phase is provoked by the material

hardening of the solid cell wall material. Therefore, a macroscopic hardening modulus $H^*_{1,T}$ can be given analytically for the third phase:

$$H^*_{1,T} = \left(\frac{t}{h}\right) E^s_T \tag{4.12}$$

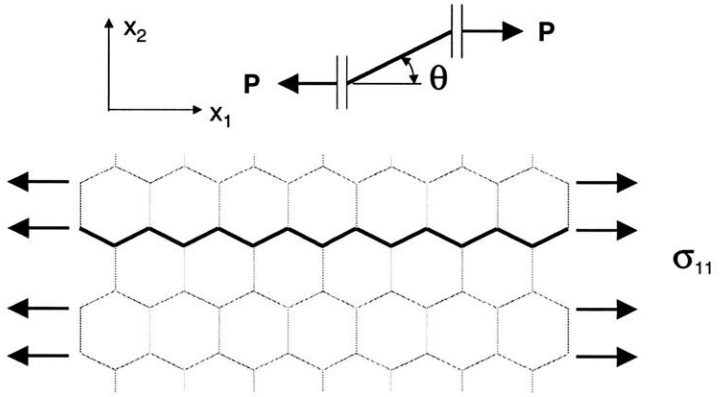

Figure 4-8: Clamped beam as representative microstructure for tension in x_1-direction

4.4.3 Compression

The macroscopic stress-strain curve for the compressive crushing in x_1-direction is plotted in figure 4-10. The details are given in appendix A.3. Qualitatively, the crushing characteristics are the same. Quantitatively, the crushing into the x_1-direction absorps approximately 20% less energy than the crushing into the x_2-direction during the crushing in the plateau regime. Since the kinematics permit a perfect folding of the honeycomb by forming plastic hinges in the cell wall corners, the densification starts very late at a macroscopic strain of approximately $\epsilon_{11} \approx 0.75$.

4.4.4 Kinematics and transformation to volumetric strains

Analogous to the crushing in x_2-direction, the kinematics for the crushing in x_1-direction are developed. The simplified kinematical model is sketched in figure 4-11. The assumptions match

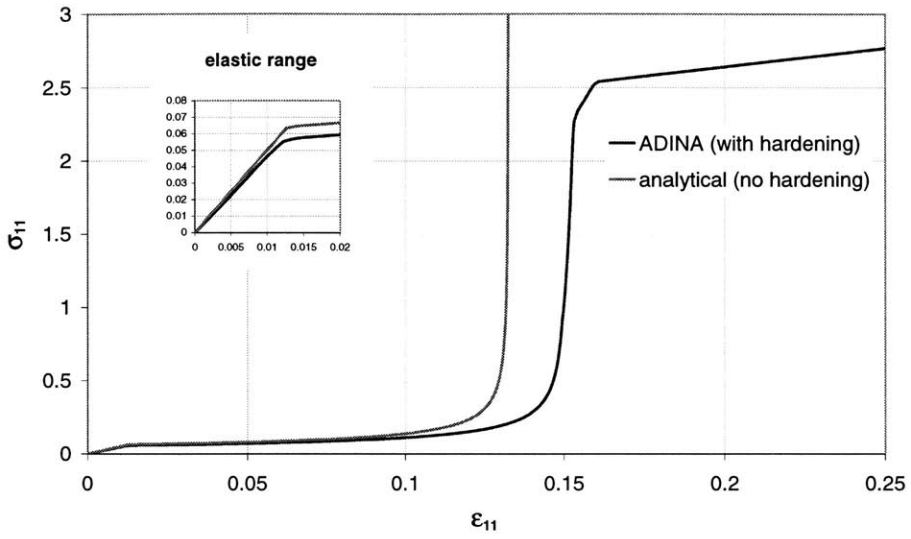

Figure 4-9: Macroscopic stress-strain curve for tension in x_1-direction

with the assumptions made for the x_2-direction for $\theta > 0$. In this case, $\theta > \theta_0$ corresponds to compression and $\theta < \theta_0$ describes tension. For $\theta = 0$, the height of the representative cross-section area remains constant while the strains in x_1-direction grow. The following expressions for the volumetric strain as a function of the macroscopic strain ϵ_{11} are obtained:

$$\epsilon_v = 1 - \frac{\left(\frac{h}{l}\right) + sin\left\{arccos[cos\theta_0(\epsilon_{11}+1)]\right\}}{\left(\frac{h}{l}\right) + sin\theta_0}(\epsilon_{11}+1), \qquad \theta > 0 \tag{4.13}$$

$$\epsilon_v = \frac{lsin\theta_0 - h\epsilon_{11}}{h + lsin\theta_0}, \qquad \theta = 0 \tag{4.14}$$

The equation (4.13) is plotted in figure 4-12. The curve changes twice its monotony and shows negative volumetric strains for large macroscopic tensile strains. Therefore, the mapping of the macroscopic strains ϵ_{11} into the space of the volumetric strains is injective for all ϵ_{11} outside the intervall that is defined by the two roots. Concerning the transformation of a stress-strain curve into a stress-volumetric strain curve, only the information about the tensile test between the two roots is lost and cannot be included into the material model 26 in LS-DYNA.

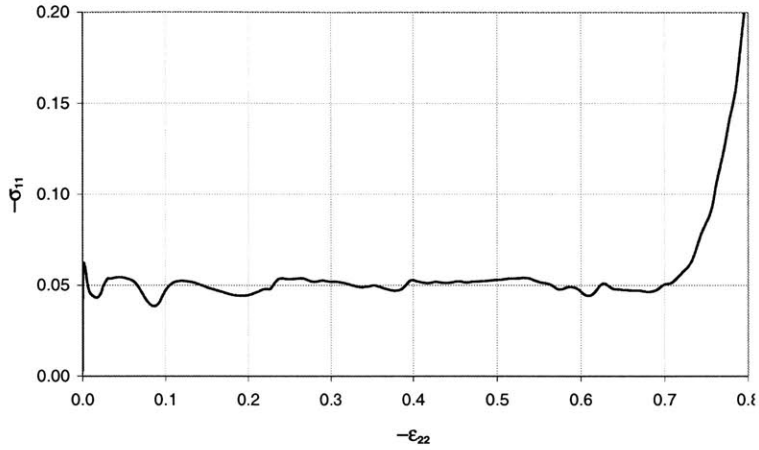

Figure 4-10: Macroscopic stress-strain curve for compressive crushing in x_1-direction

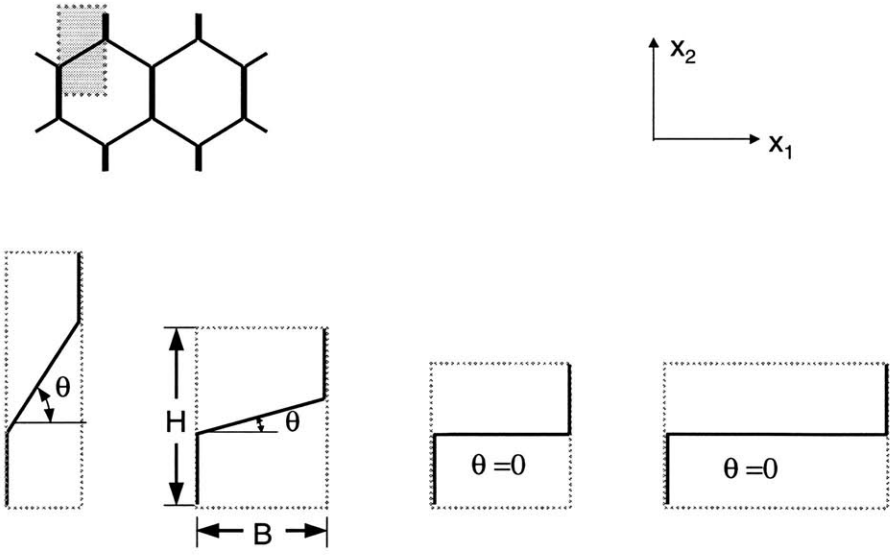

Figure 4-11: Simplified kinematics of the crushing in x_1-direction

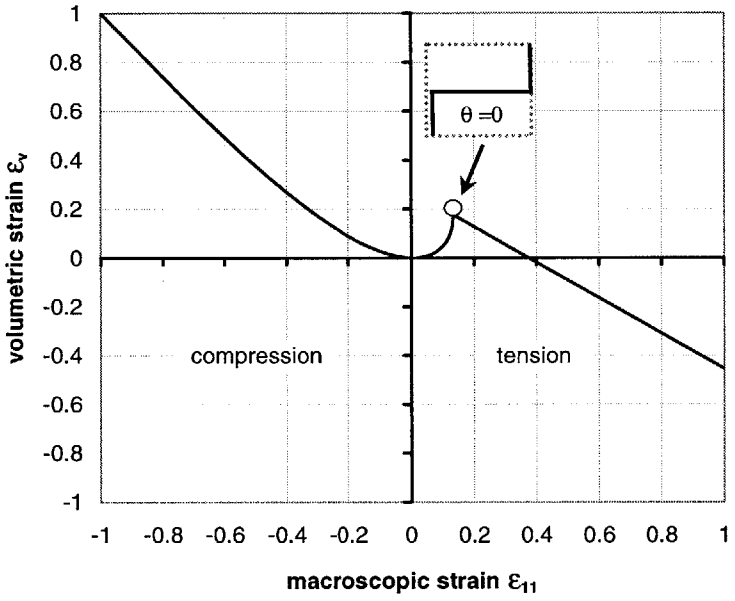

Figure 4-12: Relationship between the volumetric strain ϵ_v and the macroscopic strain ϵ_{11}

4.5 Shear Crushing in the x_1-x_2-plane

4.5.1 Shear Modulus G_{12}^*

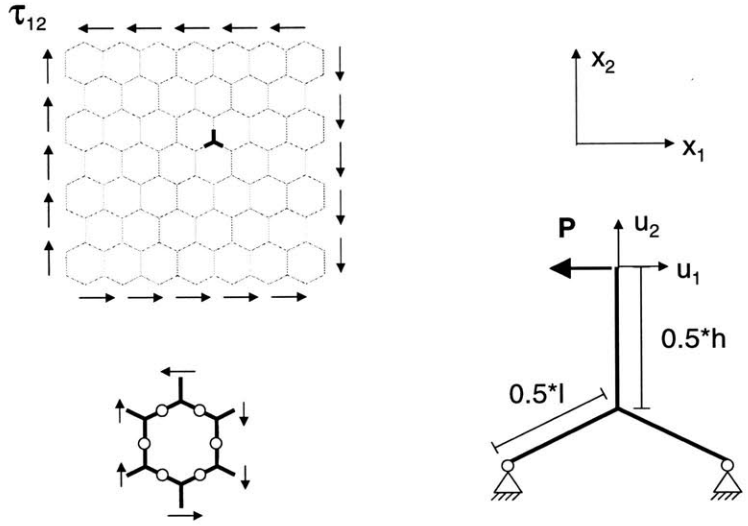

Figure 4-13: Mechanical system for the evaluation of the macroscopic material properties for in-plane shear

In the case of in-plane shear, the double-thickness cell walls are very important. The mechanical system used to evaluate the shear behaviour of the honeycomb is given in figure 4-13. The shear loading consists of two anti-symmetric loadings, that allow the reduction of the full cross-section to the characteristic Y-element. Since the momentum distribution for an anti-symmetric loading of a symmetric system is anti-symmetric and therefore equals zero in the middle lines of the cell-walls. Applying elastic beam theory to the triad shown in figure 4-13, the following expression for the shear modulus G_{12}^* is obtained:

$$G_{12}^* = \left(\frac{t}{l}\right)^3 \frac{sin\theta + \frac{h}{l}}{cos\theta \left(\frac{h}{l}\right)^2 \left(1 + \frac{h}{4l}\right)} \tag{4.15}$$

The value of G_{12}^* is approximately 2 MPa for the given honeycomb. This is more than twice as high as the shear modulus of the corresponding monolithic honeycomb without double-thickness walls.

4.5.2 Large Deformation due to Shear

The inelastic macroscopic properties for in-plane shear are determined by a nonlinear analysis of the triad presented before 4-13. The resulting force curve $P(u_1, u_2)$, where u_1 and u_2 are the in-plane displacements as drawn in figure 4-13, is translated into a the shear stresses τ_{12} as a function of the distorsion γ_{12}:

$$\tau_{12} = \frac{P}{2lcos\theta} \qquad \text{and} \qquad \gamma_{12} = \frac{|u_1|}{0.5(h + lsin\theta) + u_2} \tag{4.16}$$

This curve is shown in figure 4-15. The reliability of that curve is limited to $\gamma_{12} < 20$, because the thin cell wall deflections become so large, that the double-thickness wall touches the thin wall. Figure 4-14 shows the deformed cross-section in a configuration that is close to that limit state. Since contact between cell walls is not included in the ADINA beam model, densification can not be modeled for large shear deformations with this analysis.

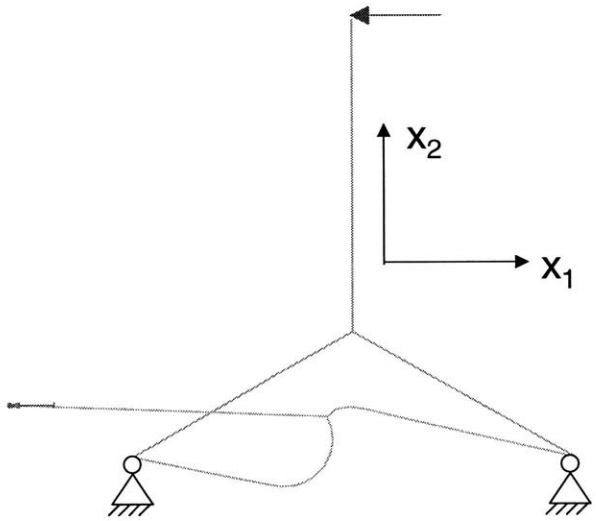

Figure 4-14: Large deformed mircostructure due to in-plane shear τ_{12}

4.5.3 Kinematics and Transformation to Volumetric Strains

The transformation to volumetric strains is directly performed on the basis of the simulation results of ADINA. Following the basic assumption of the analysis, that the distance between the points A

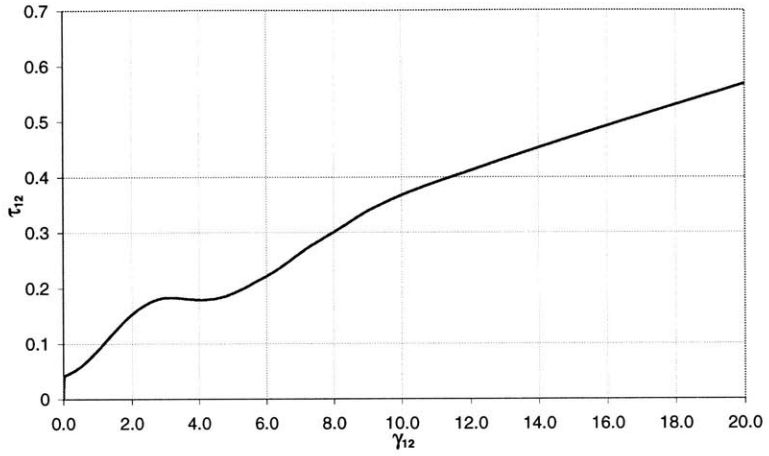

Figure 4-15: Macroscopic stress-distorsion curve for shear in the (x_1, x_2)-plane

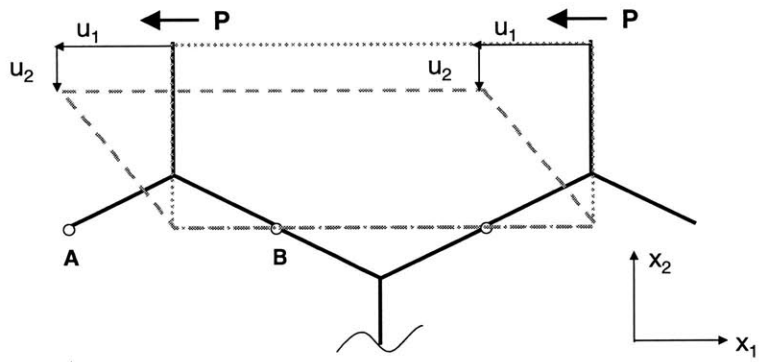

Figure 4-16: Kinematics for the transformation to volumetric strains for shear deformations in the (x_1, x_2)-plane, control volume with dashed line

and B remains constant during the shear deformation [3](see fig. 4-16), the volumetric strains can be expressed as a function of the in-plane displacements u_2:

$$\epsilon_v = -\frac{2u_2}{h + lsin\theta_0} \tag{4.17}$$

4.6 Shear Crushing in the x_1-x_3-plane

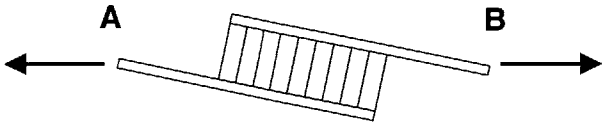

Figure 4-17: Tensile Plate Shear Tests, Hexcel/MIT 1997

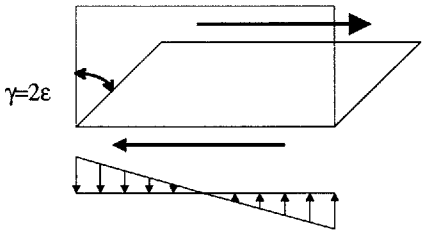

Figure 4-18: Shear test: Shear, tension and compression introduced

In material tests presented in the previous sections, it was easy to perform a test, that introduced only stresses that corresponded to the material properties that was looked for. In shear tests, the introduction of shear only can be very difficult. A serious problem in experimental tests that were performed by Hexcel was the failure of the interface between the honeycomb core and the top plates that were glued onto the honeycomb to apply the shear loading (see fig. 4-17). It must be noted, that this failure can be excluded in a numerical test, but the problem of normal stresses, that are introduced at the outer surfaces would still be present.

Thus, even the design of the optimal numerical test in order to determine the shear properties in the x_1-x_3-plane is very difficult, because the idealized test as it was performed for the in-plane shear properties cannot be performed; this kind of test, that introduces shear only, shows difficulties because of the local properties at that point where the shear is introduced would dominate the global response.

The idealized mechanical system of the test performed by Hexcel is sketched in figure 4-18. The difference between the idealized and the "real" test is, that the two loading points A and B (fig. 4-17) are thought to be infinitely far away in the idealized test. But still, normal stresses as they are sketched in fig. 4-18 would be introduced into the specimen. From a first approximation (Bernoulli

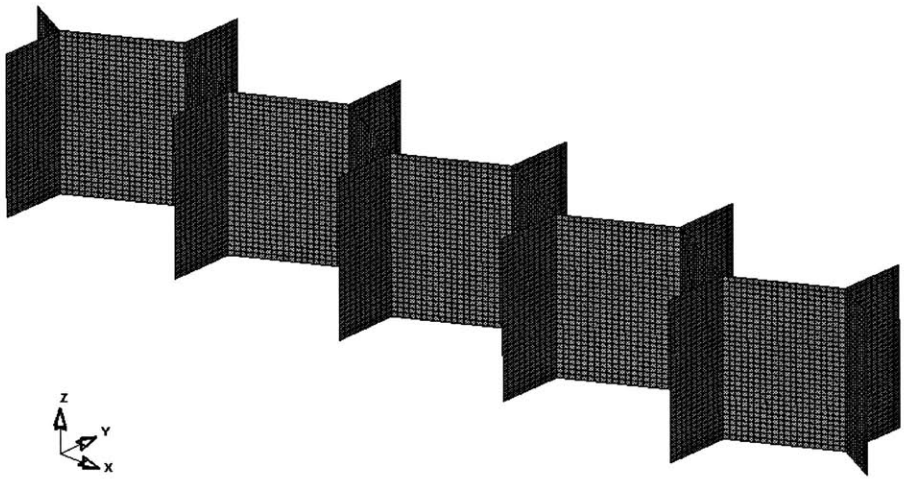

Figure 4-19: Numerical shear test of honeycomb: Initial configuration, 9900 bilinear shell elements

beam theory), it can be seen that the maximum compression and tension stresses are proportional to $\frac{H}{L^2}$, where H denotes the height and L the length of the specimen. This means, that the perfect specimen would have to be infinitely long in order to make sure that no normal stresses are introduced.

Of course, a numerical shear test of an infinitely specimen can not be considered. In this study, a specimen with a height of $5mm$ and a length of $28.3mm$ is subjected to a horizontal displacement of his top surface (fig. 4-19).

4.6.1 Shear Modulus G^*_{13}

A simple formula to evaluate the shear modulus in the x_1-x_3 plane is given by Kelsey *et al.* [8]:

$$G^*_{13} = \left(\frac{t}{l}\right) \frac{cos\theta}{(h/l + sin\theta)} G_s \tag{4.18}$$

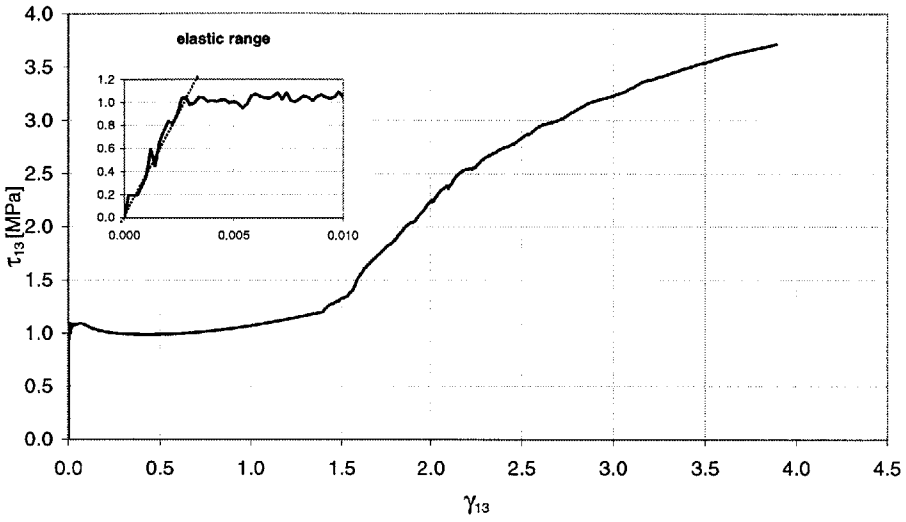

Figure 4-20: Macroscopic stress-distorsion curve for shear crushing in the x_1-x_3-plane

This delivers a shear modulus of $G^*_{13} = 420MPa$.

4.6.2 Shear Crushing

The characteristic macroscopic stress-distorsion curve is plotted in figure 4-20. Details about the analysis and plots of the deformed configurations can be found in appendix A.4. Macroscopically, three regimes characterize the shear behavior:

- linear elastic behavior; the shear modulus given by the results of the numerical simulations is approximately $G^*_{13} = 400MPa$. This corresponds very well to the value obtained from equation (4.18);
- plateau regime: The shear force applied remains almost constant; shear belts build up in each cell seperately and dominate the deformation pattern;
- densification: As the horizontal and vertical displacements approach the total initial height of the specimen, the honeycomb is highly compressed and the stiffness increases drastically;

It has been demonstrated above, the macroscopic stress-distorsion curve is not yet the intrinsic material curve that represents the shear behavior in the x_1-x_3-plane. Besides the macrsocopic

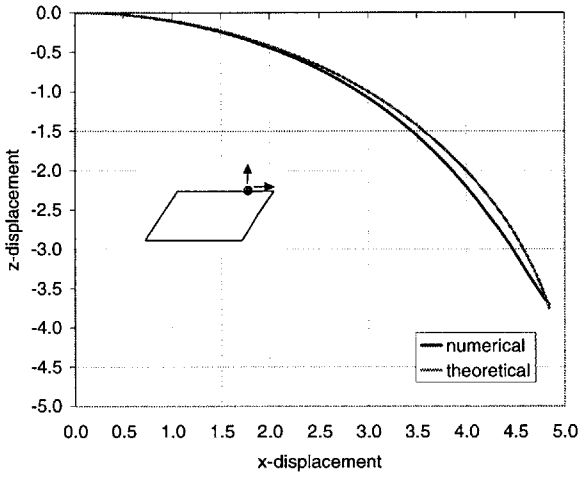

Figure 4-21: Proof of the assumption of a circular deformation path

shear properties, curve (4-20) includes the effect of normal stresses that were introduced at the bottom surface. It can be clearly seen from figures A-28 to A-30 that the microstructure fails catastrophically in those regions where the compression forces are introduced from the boundaries. Thus, the mean crushing force migth be strongly influenced by the geometry of the specimen.

4.6.3 Kinematics and Transformation to Volumetric Strains

Mocroscopically, the deformed configuration in the x_1-x_3-plane can be described as a parallelogram. The simplified kinematics assume, that the edges of this parallelogram do not change their initial length. Figure 4-21 shows, that an arbitrary point on the top surface follows a circular line during the deformation. Based on this assumption, the following relationship between the shear distorsion γ_{13} and the volumetric strains ϵ_v can be derived:

$$\epsilon_v = 1 - cos[arctan(\gamma_{13})] \tag{4.19}$$

Chapter 5

Summary

The analysis of the three-dimensional macroscopic mechanical properties of metallic honeycomb is performed using a mix of analytical and numerical methods. This master thesis demonstrates that it is feasible to use highly complex micromechanical analysises to determine the macroscopic core properties of an ultralight sandwich plate. The macroscopic stress-strain curves that describe the mechanical behavior of honeycomb for large deformations are determined independently for each component of the stress tensor. As an examplary study, the properties of a commercially available aluminium honeycomb with double thickness walls and a crushing strength of $2MPa$ are estimated.

The macroscopic response with respect to uniaxial compressive crushing, can be splitted into three regimes:

1. linear elastic behavior;
2. plateau regime;
3. densification phase;

Although the qualitative responses are the same for all three material axes, a quantitative analysis shows that the stiffness and mean crushing forces in the x_3-direction are several orders of magnitude higher than the corresponding in-plane properties in x_1- or x_2-direction. In the case of in-plane loading, the deformations of the microstructure are primarily bending dominated and higly localized in plastic hinges; as a result the dissipated energy per strain increment is low. However, deformations in the x_3-direction use the cell-walls more efficiently by folding and membrane straining; thus, the microstructural resistance is much higher.

Under unidirectional tension, the macroscopic behaviour in x_3-direction differs qualitatively from the in-plane responses. While the macroscopic behaviour in x_3-direction is proportional to the

elasto-plastic behaviour of the solid aluminium, the in-plane response is very different. In a first phase, the honeycomb hardens structurally until the bending dominated microstructure shifts into a membrane dominated system, where the macroscopic stresses reach the same order of magnitude as the stresses in the microstructure;

In a first approximation hexagonal honeycomb might be assumed to behave transversely isotropic. But it must be noted that, when the macroscopic response changes from structural to material hardening, the strain level can be very different for both in-plane directions.

Shear deformation always yields volumetric material compression. In the case of out-of-plane shear crushing, the honeycomb responds with a mean crushing stress that is approximately half of the out-of-plane compression crushing stress. After a 40% volumetric compression, the stresses increase smoothly until the honeycomb is completely compacted. When the honeycomb is subjected to in-plane shear, no plateau regime is present and the honeycomb hardens with a macroscopic shear tangent modulus ($G^*_{12,T} \approx G^*_{12}/100$).

Bibliography

[1] K.-J. Bathe. *Finite Element procedures.* Prentice Hall, 1996.

[2] D.P. Flanagan and T. Belytschko. A uniform strain hexahedron and quadrilateral with orthogonal hourglass control. *International journal for numerical methods in engineering*, 17:679–706, 1981.

[3] L.J. Gibson and M.F. Ashby. *Cellular solids.* Cambridge University Press, 1997.

[4] J. O. Hallquist. *Ls-DYNA Theoretical Manual.* Livermore Software Technology Corporation, 1998.

[5] D. Mohr. *Study of the behavior of the default shell element formulations in ADINA and LS-DYNA in quasi-static analysis.* Term Project for course 2.094, Massachusetts Institute of Technology, 2000.

[6] P. Seggewiss. Numerical study of aluminum honeycomb. Master's thesis, Bundeswehr University Munich, 1996.

[7] S.D. Papaka and S. Kyriakides. In-plane compressive response and crushing of honeycomb. *Journal of the Mechanics of the Physics and the Mechnics of Solids*, 42(10):1499–1532, 1994.

[8] R.A. Gellatly S. Kelsey and B.W. Clark. *Aircraft Engineering.* p. 294, 1958.

[9] S.P. Santosa. *Crashworthiness Analysis of Ultralight Metal Structures.* PhD thesis, Massachusetts Institute of Technology, 1999.

[10] L.E. Schwer and R.G. Whirley. Lessons lerned in modeling a moving deformable barrier (mdb) impacting a rigid wall. In J.D. Reid, editor, *Crashworthiness and occupant protection in transportation systems*, pages 307–329. ASME, 1995.

[11] T. Wierzbicki. Crushing analysis of metal honeycombs. *International Journal of Impact Engineering*, 1(2):157–174, 1983.

Appendix A

Numerical Crushing of the Microstructure of Honeycomb

A.1 Compressive Crushing in x_3-direction

A.1.1 Input of the numerical model

- 990 Belytschko-Lin-Tsay shell elements, (NIP=5, IHQ=4)
- max. crushing velocity: 1000 mm/s, mass scaled solution (DT2MS=1E-7s, $\rho_{ini} = .279E - 8t/mm^3$);
- solid material: elastic-plastic, isotropic hardening (bilinear law: E=70 GPa, E_T=100 MPa, ν=0.33)
- boundary conditions: free at top, clamped on bottom, symmetry on sides;
- total CPU-time: 1305 s (Intel Celeron 466, 96 MB); Data: asemth0.dyn, firm.xls

A.1.2 Results

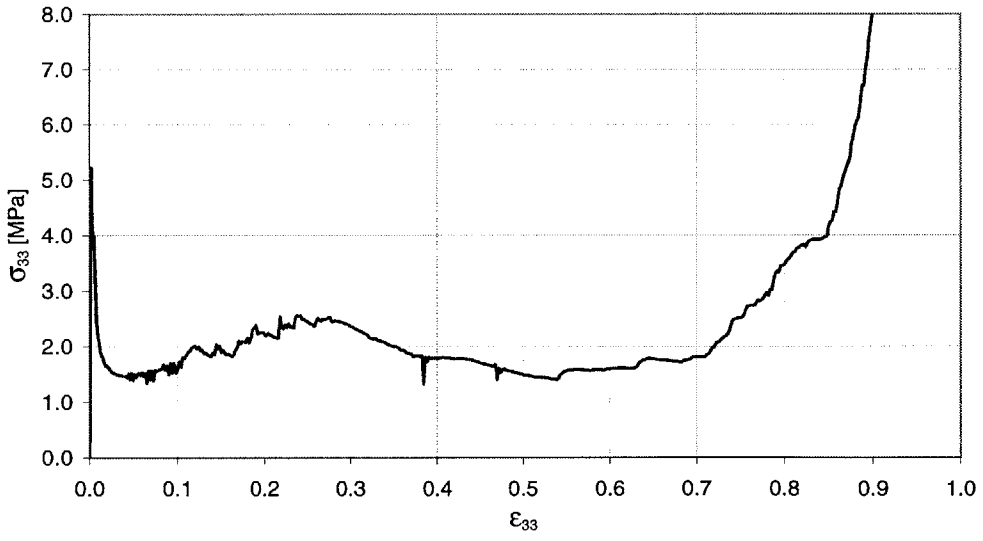

Figure A-1: Macroscopic stress-strain curve for compressive crushing in x_3-direction

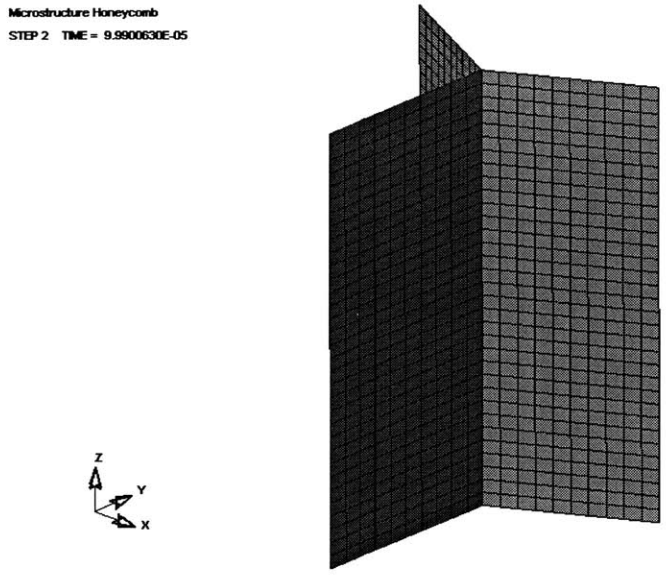

Figure A-2: Initial configuration

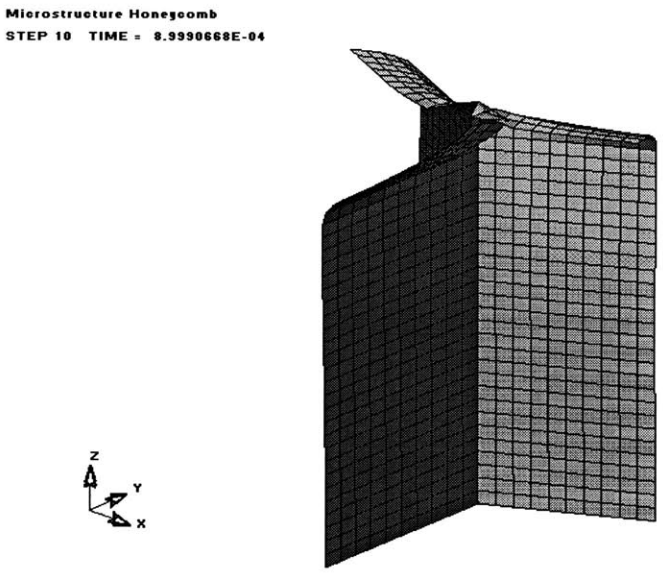

Figure A-3: Collapsed configuration for the macroscopic strain $\epsilon_{33} = 7.82\%$

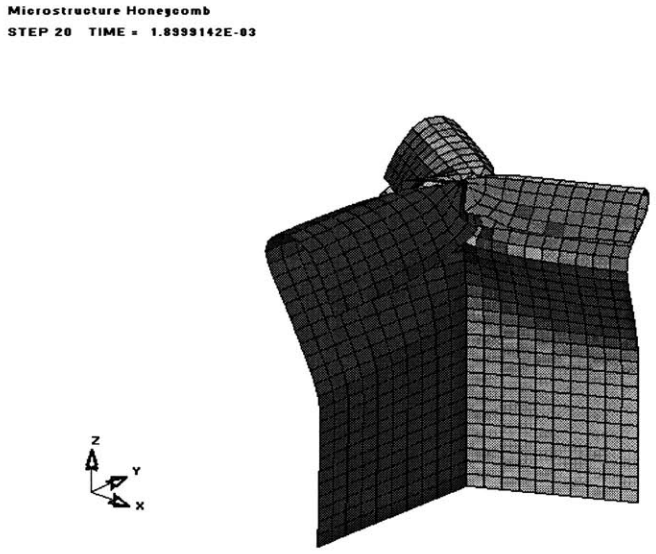

Figure A-4: Collapsed configuration for the macroscopic strain $\epsilon_{33} = 27.8\%$

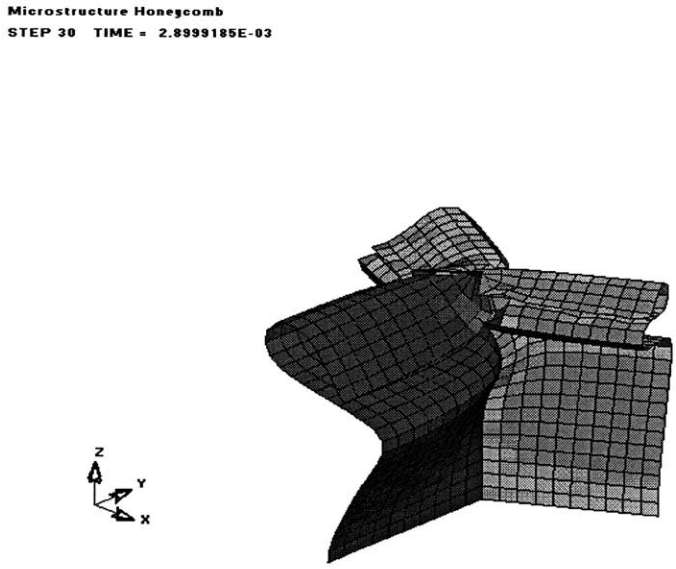

Figure A-5: Collapsed configuration for the macroscopic strain $\epsilon_{33} = 47.8\%$

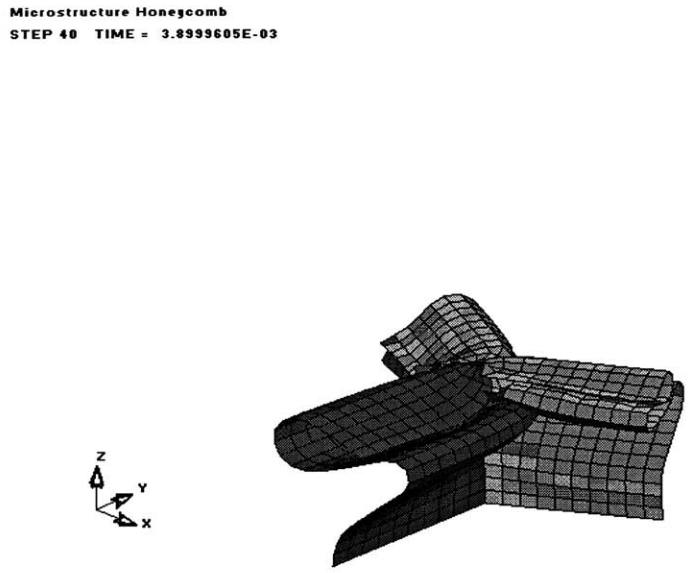

Figure A-6: Collapsed configuration for the macroscopic strain $\epsilon_{33} = 67.8\%$

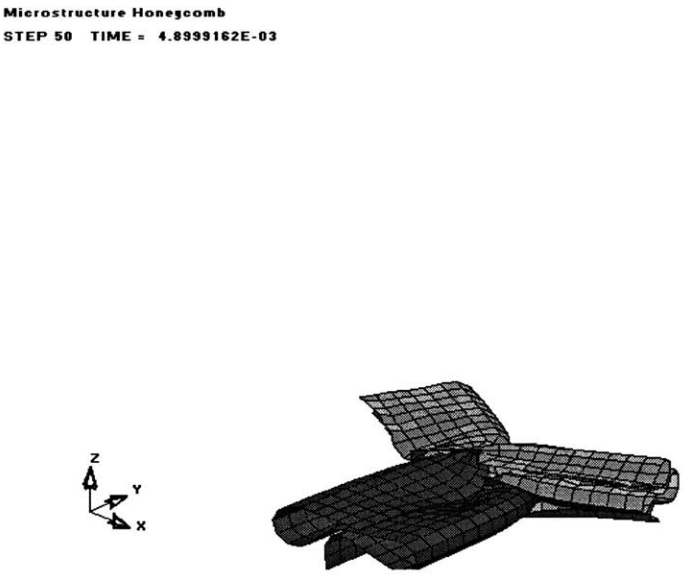

Figure A-7: Collapsed configuration for the macroscopic strain $\epsilon_{33} = 87.8\%$

A.2 Compressive Crushing in x_2-direction

A.2.1 Input of the numerical model

- 3300 Belytschko-Lin-Tsay shell elements, (NIP=5, IHQ=4)
- max. crushing velocity: 1000 mm/s, mass scaled solution (DT2MS=5E-8s, $\rho_{ini} = .279E - 8t/mm^3$);
- solid material: elastic-plastic, isotropic hardening (bilinear law: E=70 GPa, E_T=100 MPa, ν=0.0)
- boundary conditions: rigid wall on top & bottom (x-z-plane), 3 DOF only: u_x, u_y, θ_z;
- total CPU-time: 80057 s (Intel Celeron 466, 96 MB); Data: hc2c.dyn, hc2c.xls

A.2.2 Results

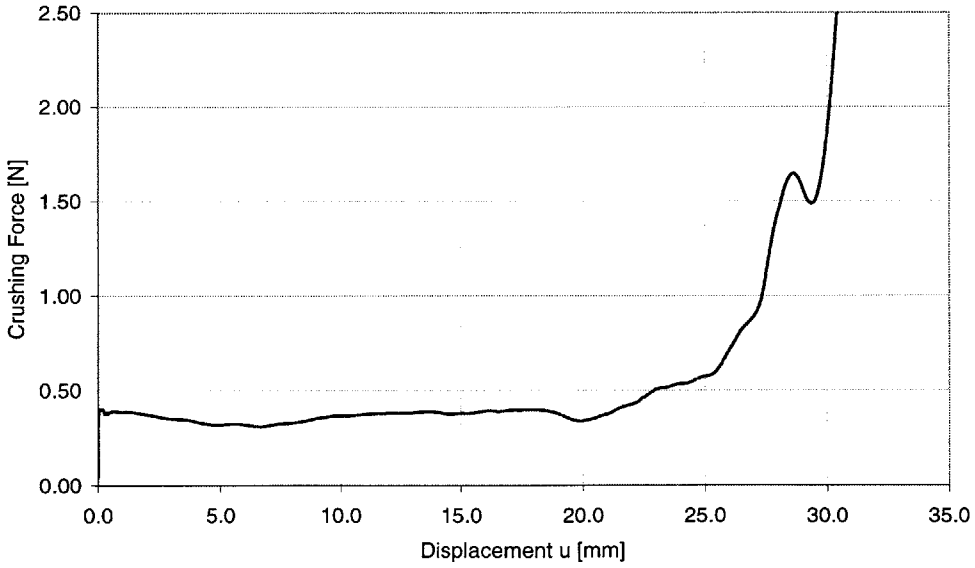

Figure A-8: Macroscopic force-displacement diagram for compressive crushing in the x_2-direction

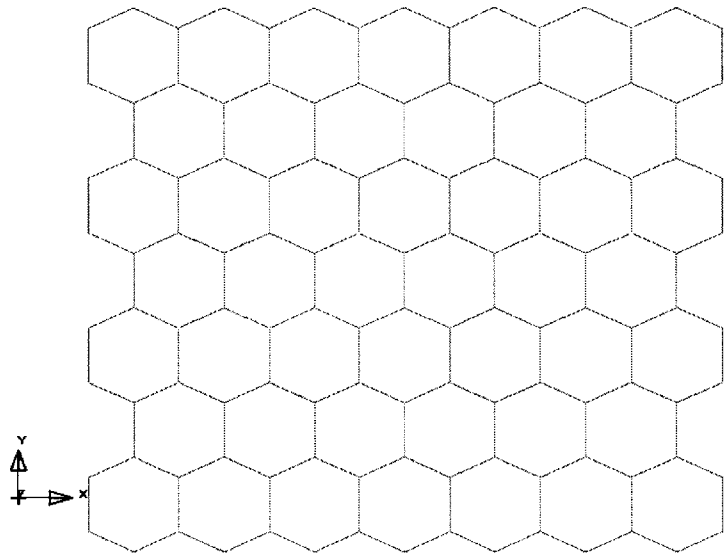

Figure A-9: Initial configuration

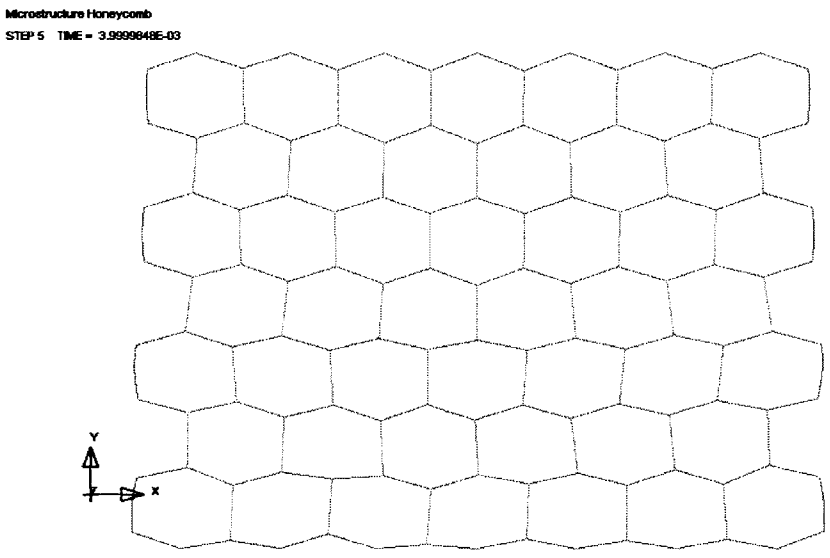

Figure A-10: Collapsed configuration for the macroscopic strain $\epsilon_{22} = 1.25\%$

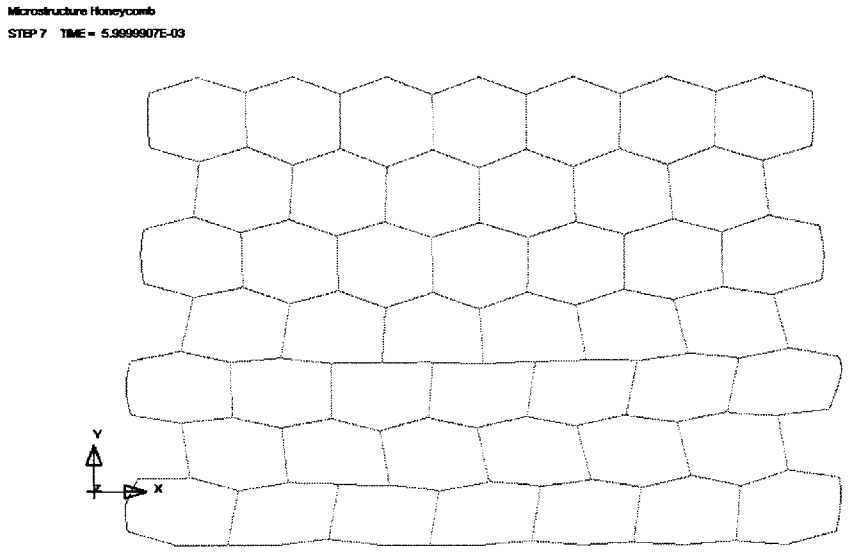

Figure A-11: Collapsed configuration for the macroscopic strain $\epsilon_{22} = 3.75\%$

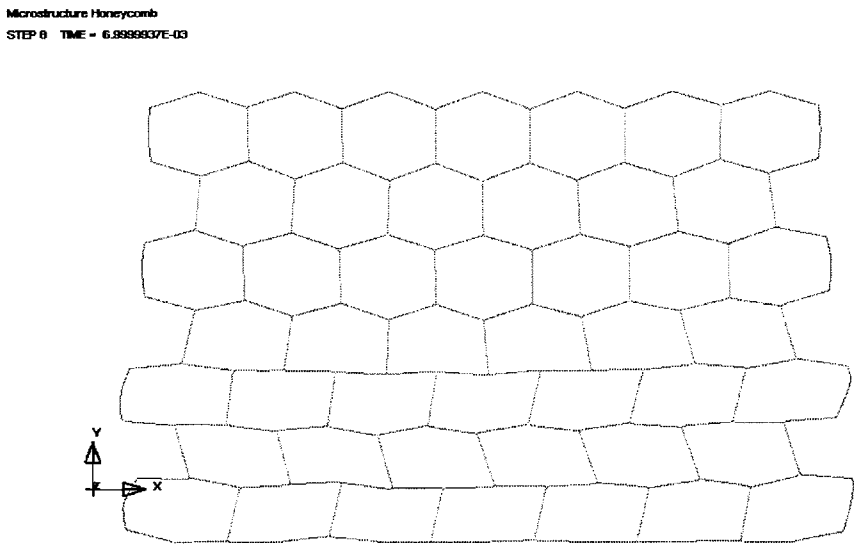

Figure A-12: Collapsed configuration for the macroscopic strain $\epsilon_{22} = 5.5\%$

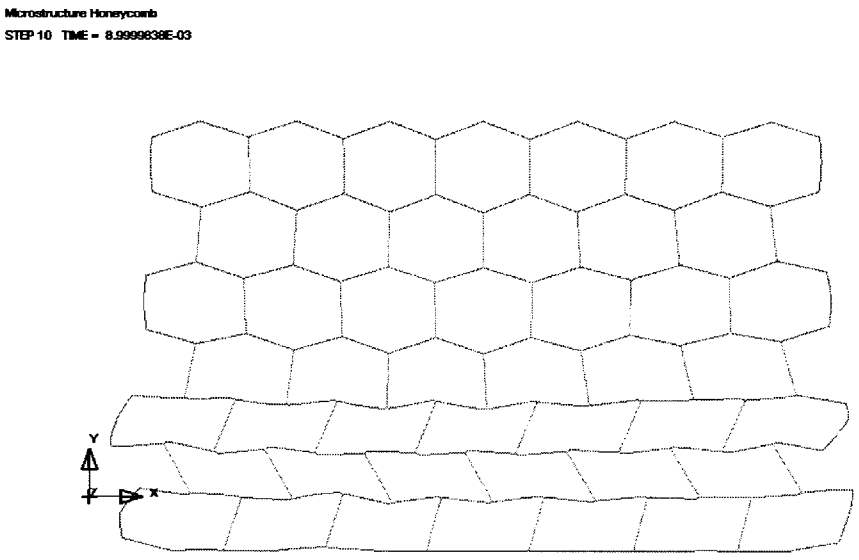

Figure A-13: Collapsed configuration for the macroscopic strain $\epsilon_{22} = 10\%$

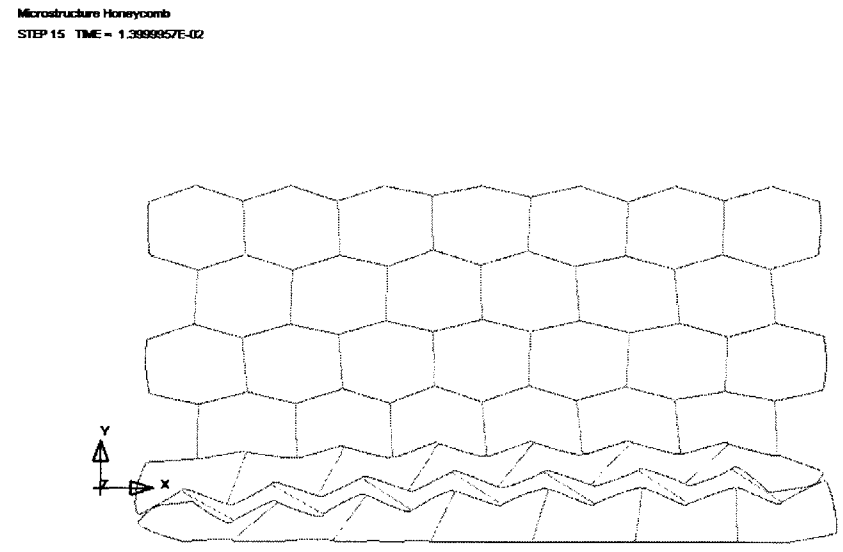

Figure A-14: Collapsed configuration for the macroscopic strain $\epsilon_{22} = 22\%$

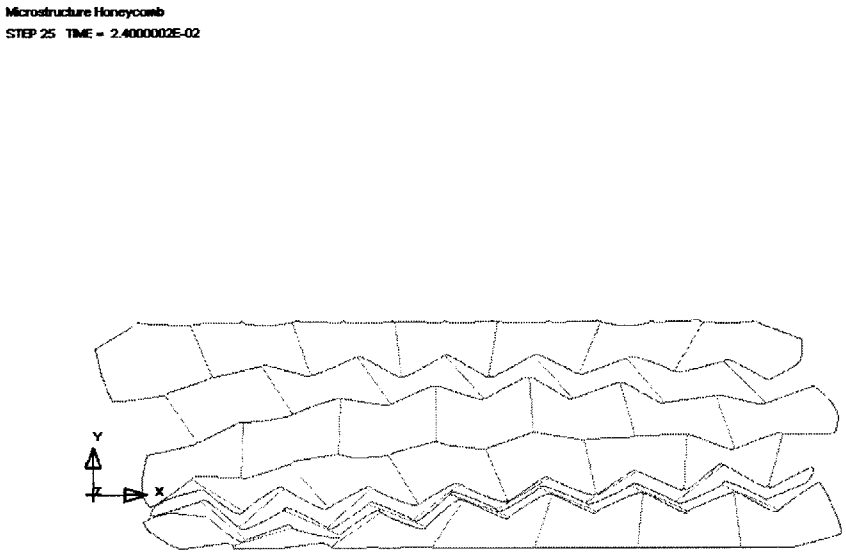

Figure A-15: Collapsed configuration for the macroscopic strain $\epsilon_{22} = 47.5\%$

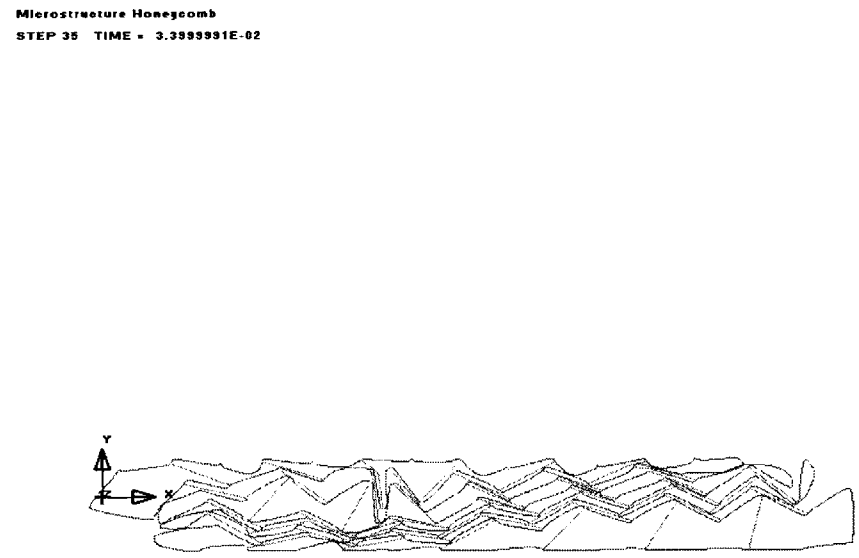

Figure A-16: Collapsed configuration for the macroscopic strain $\epsilon_{22} = 72\%$

A.3 Compressive Crushing in x_1-direction

A.3.1 Input of the numerical model

- 3300 Belytschko-Lin-Tsay shell elements, (NIP=5, IHQ=4)
- max. crushing velocity: 1000 mm/s, mass scaled solution (DT2MS=5E-8s, $\rho_{ini} = .279E - 8t/mm^3$);
- solid material: elastic-plastic, isotropic hardening (bilinear law: E=70 GPa, E_T=100 MPa, ν=0.0)
- boundary conditions: rigid wall on left & right (x-z-plane), 3 DOF only: u_x, u_y, θ_z;
- total CPU-time: 77633 s (Intel Celeron 466, 96 MB); Data: hc1c.dyn, hc1c.xls

A.3.2 Results

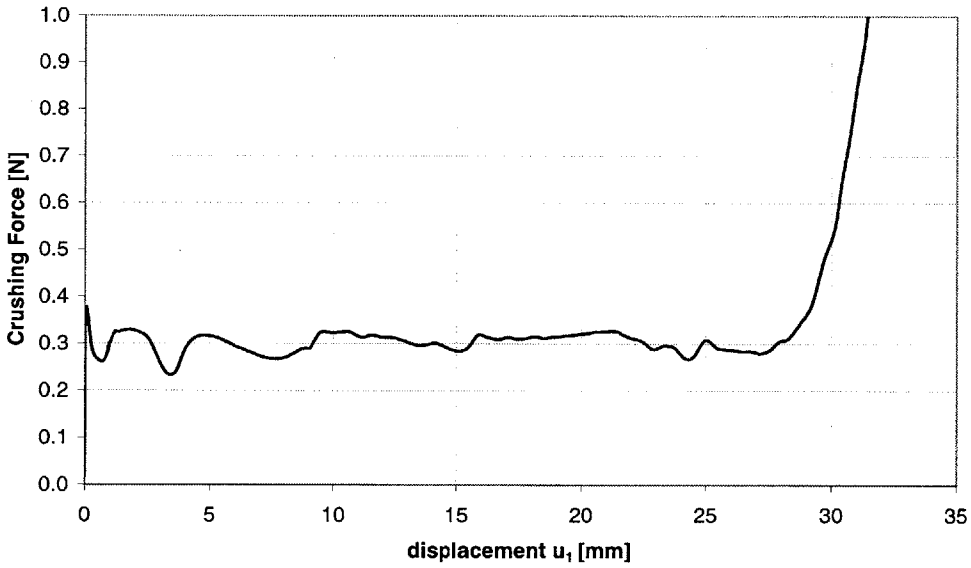

Figure A-17: Macroscopic force-displacement diagram for compressive crushing in the x_1-direction

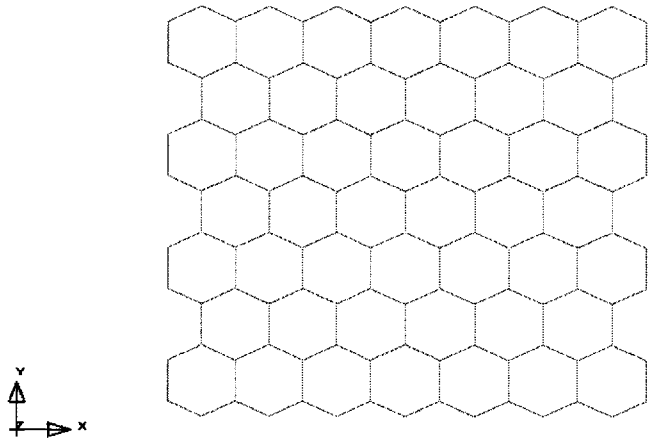

Figure A-18: Initial configuration

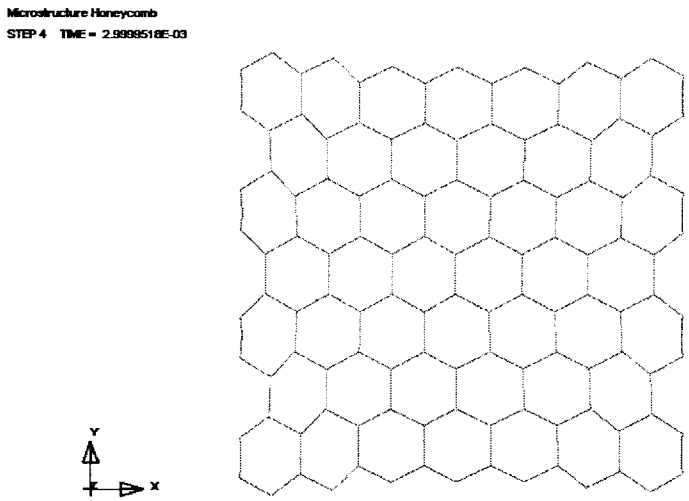

Figure A-19: Collapsed configuration for the macroscopic strain $\epsilon_{11} = 0.56\%$

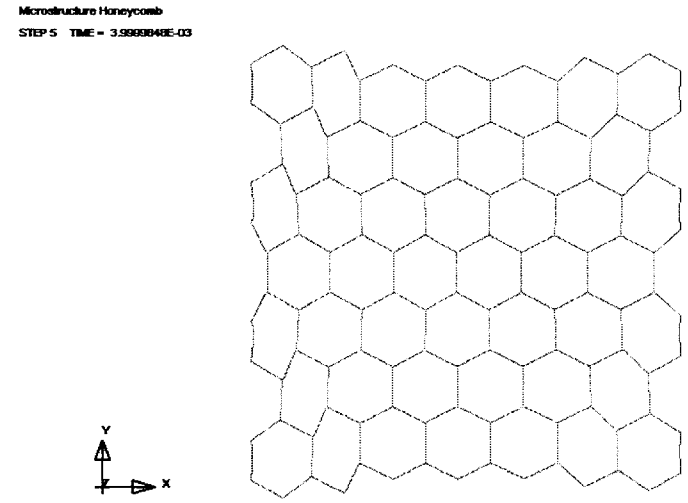

Figure A-20: Collapsed configuration for the macroscopic strain $\epsilon_{11} = 1.25\%$

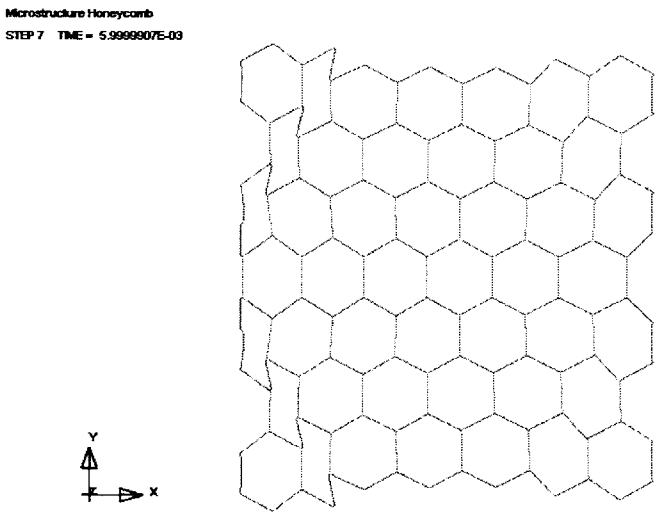

Figure A-21: Collapsed configuration for the macroscopic strain $\epsilon_{11} = 3.75\%$

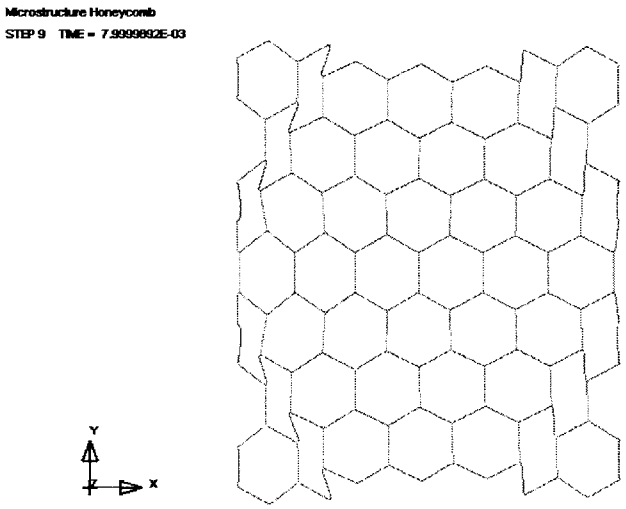

Figure A-22: Collapsed configuration for the macroscopic strain $\epsilon_{11} = 7.7\%$

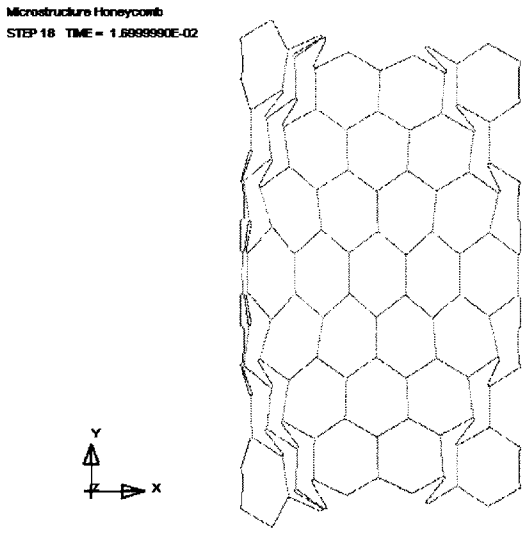

Figure A-23: Collapsed configuration for the macroscopic strain $\epsilon_{11} = 30\%$

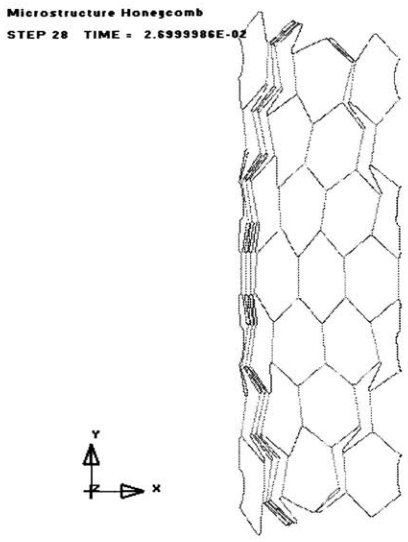

Figure A-24: Collapsed configuration for the macroscopic strain $\epsilon_{11} = 54\%$

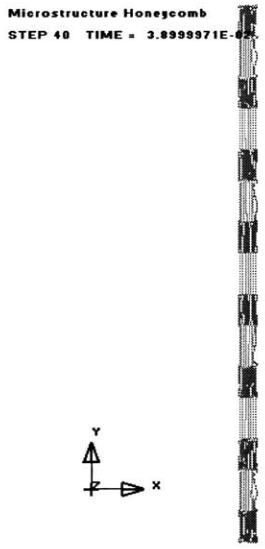

Figure A-25: Collapsed configuration for the macroscopic strain $\epsilon_{11} = 85\%$

A.4 Shear crushing in the x_1-x_3-plane

A.4.1 Input of the numerical model

- 9900 Belytschko-Lin-Tsay shell elements, (NIP=5, IHQ=4)
- max. crushing velocity: 1000 mm/s, $\rho = .279E - 8t/mm^3$;
- solid material: elastic-plastic, isotropic hardening (bilinear law: E=70 GPa, E_T=100 MPa, ν=0.33)
- boundary conditions: displacements fixed at bottom, rigidly coupled z-DOF at top, symmetry for sides in x-z-plane, free for sides in y-z-plane;
- total CPU-time: 62776 s (Intel Celeron 466, 96 MB); Data: ahc13sp.dyn, shear13.xls

A.4.2 Results

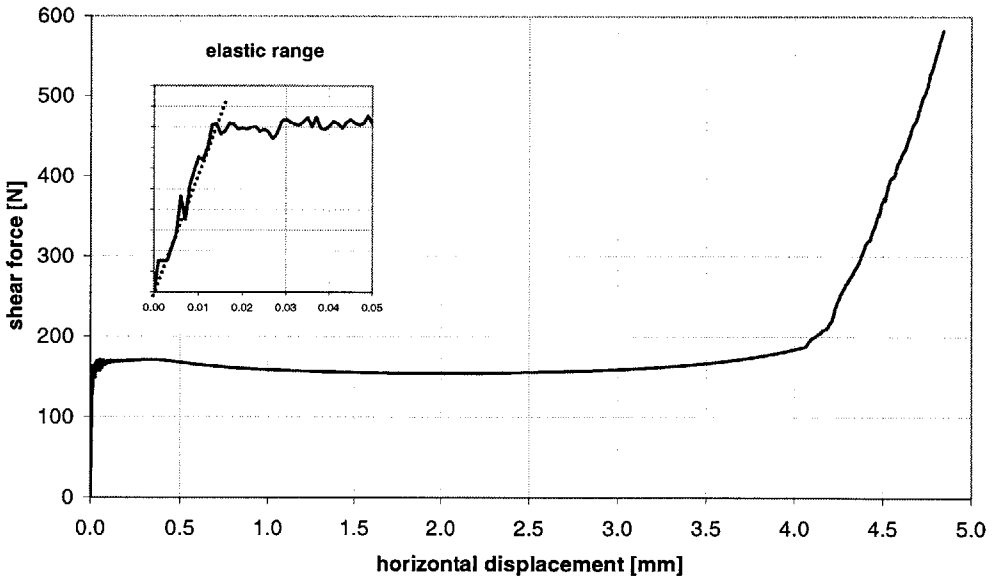

Figure A-26: Macroscopic force-displacement diagram for shear crushing in the x_1-x_3-plane

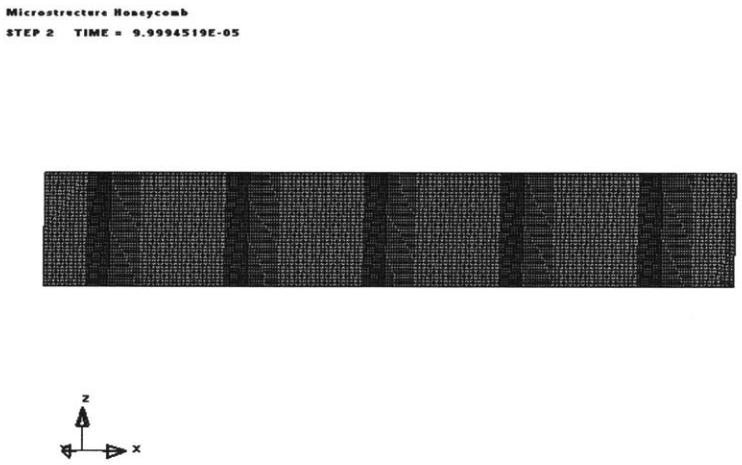

Figure A-27: Initial configuration

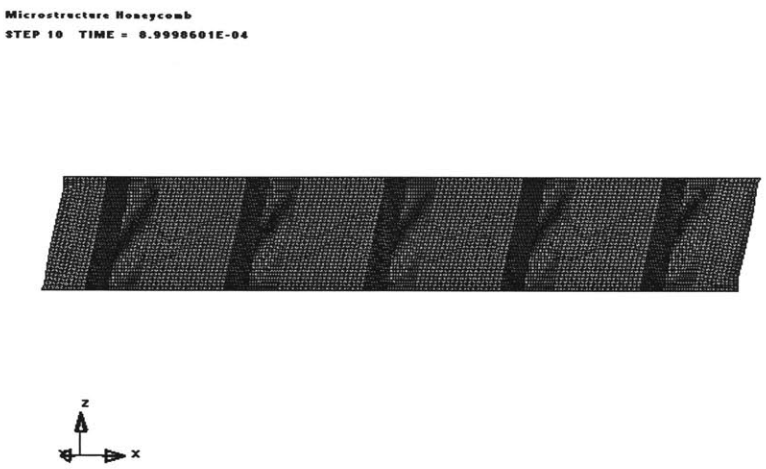

Figure A-28: Collapsed configuration for the macroscopic distorsion $\gamma_{13} = 0.2$

Figure A-29: Collapsed configuration for the macroscopic distorsion $\gamma_{13} = 0.4$

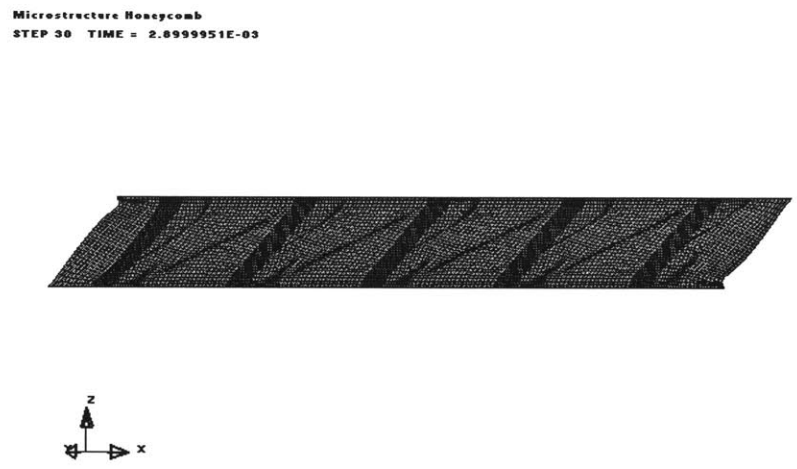

Figure A-30: Collapsed configuration for the macroscopic distorsion $\gamma_{13} = 0.7$

Figure A-31: Collapsed configuration for the macroscopic distorsion $\gamma_{13} = 1.2$

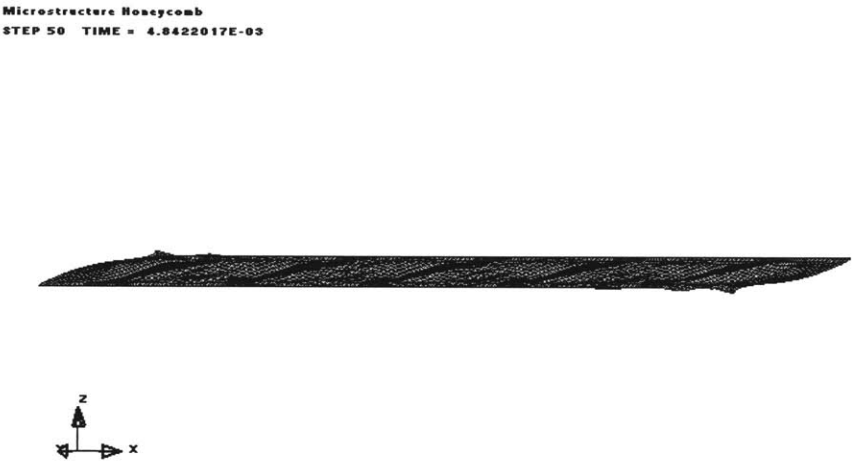

Figure A-32: Collapsed configuration for the macroscopic distorsion $\gamma_{13} = 3.6$

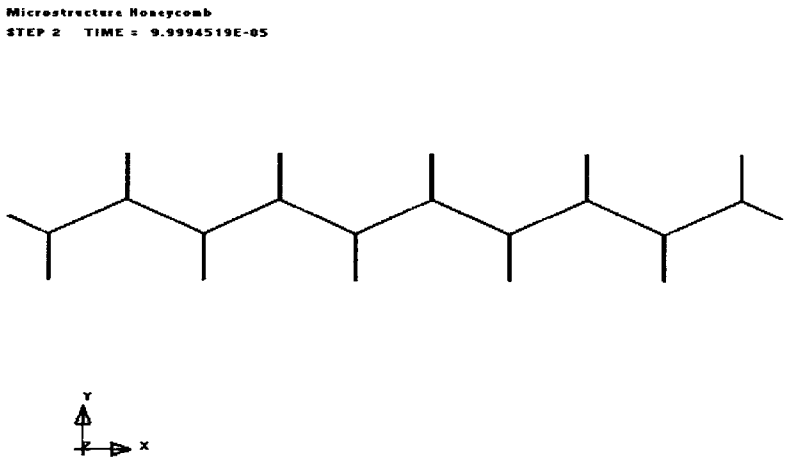

Figure A-33: Initial configuration

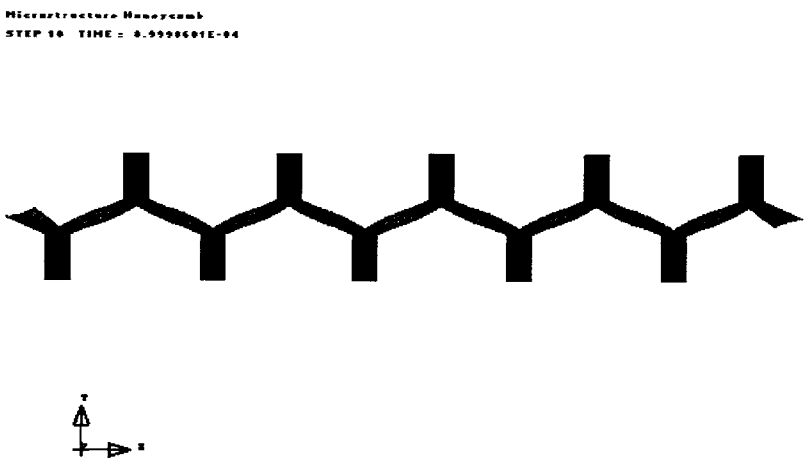

Figure A-34: Collapsed configuration for the macroscopic distorsion $\gamma_{13} = 0.2$

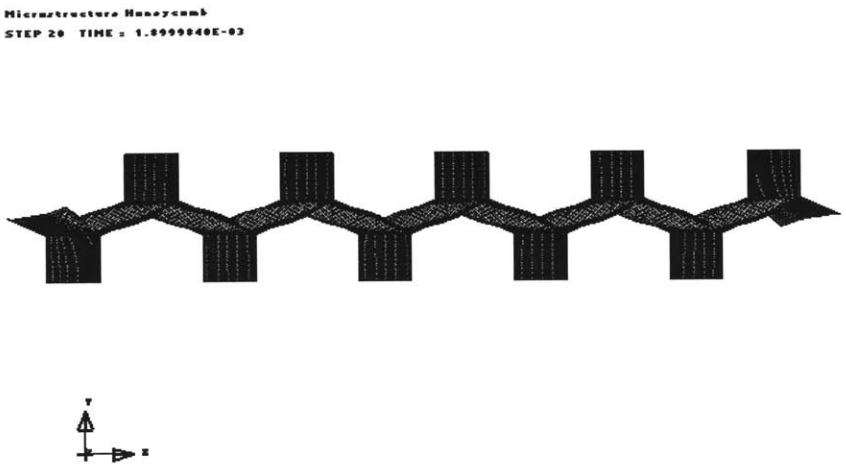

Figure A-35: Collapsed configuration for the macroscopic distorsion $\gamma_{13} = 0.4$

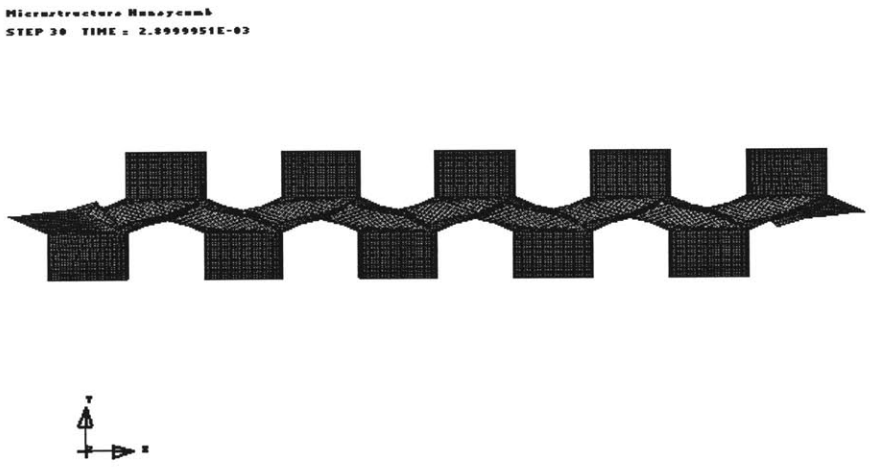

Figure A-36: Collapsed configuration for the macroscopic distorsion $\gamma_{13} = 0.7$

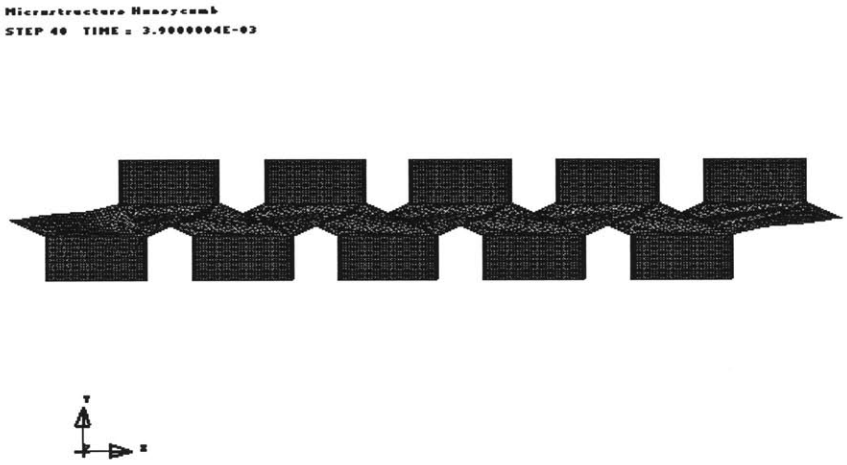

Figure A-37: Collapsed configuration for the macroscopic distorsion $\gamma_{13} = 1.2$

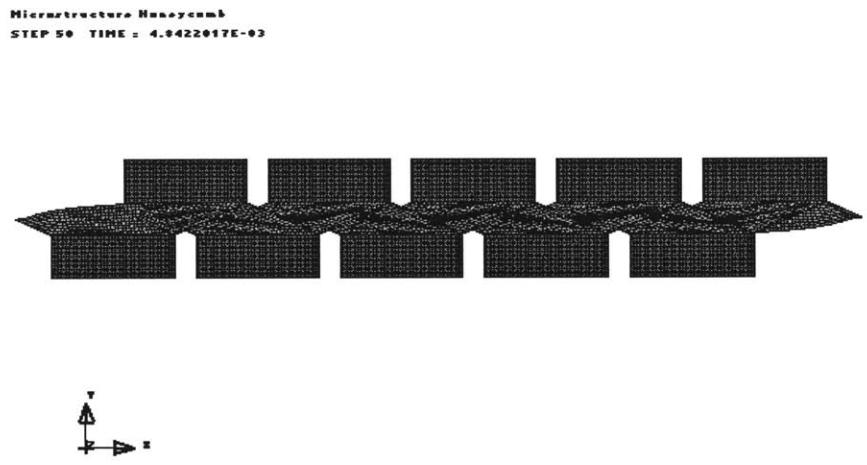

Figure A-38: Collapsed configuration for the macroscopic distorsion $\gamma_{13} = 3.6$

Appendix B

Macroscopic Material behavior as a function of the volumetric strain

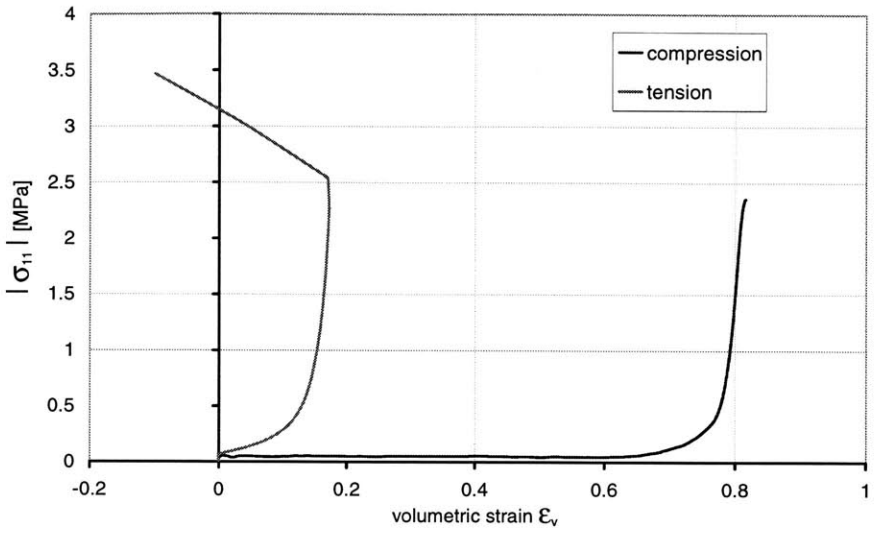

Figure B-1: Macroscopic stress σ_{11} as function of the volumetric strain ϵ_v

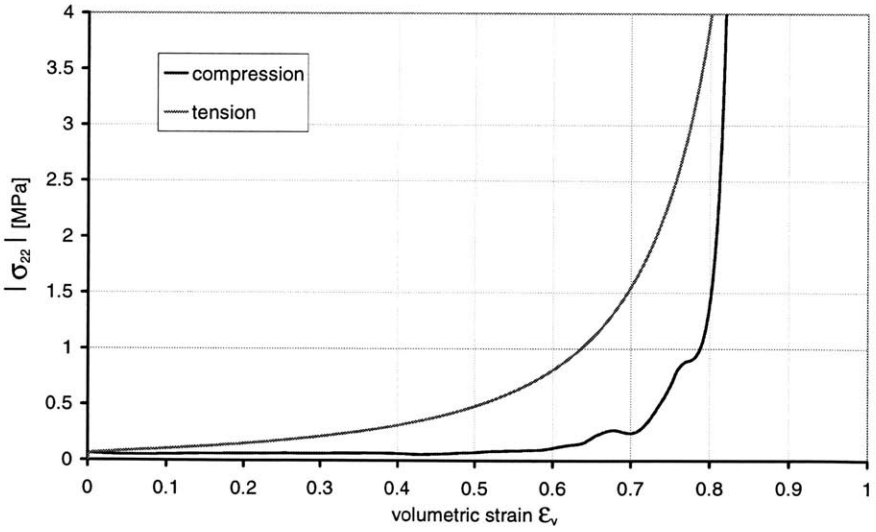

Figure B-2: Macroscopic stress σ_{22} as function of the volumetric strain ϵ_v

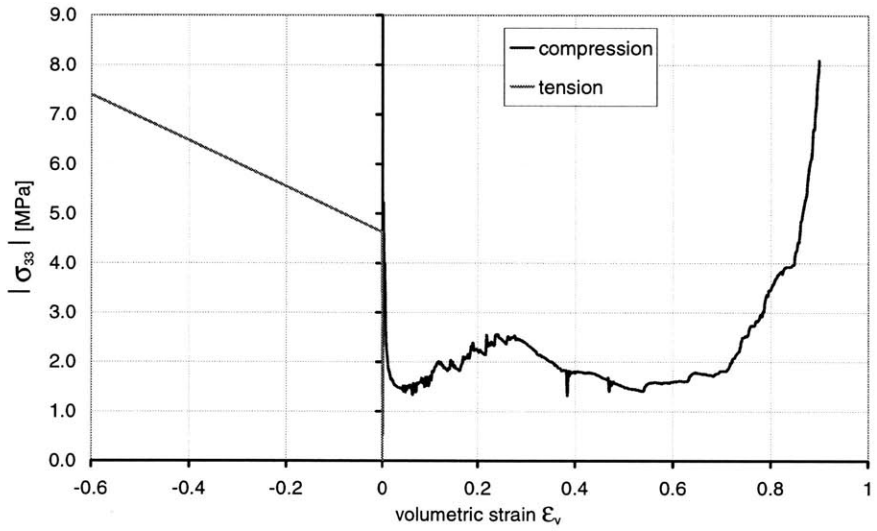

Figure B-3: Macroscopic stress σ_{33} as function of the volumetric strain ϵ_v

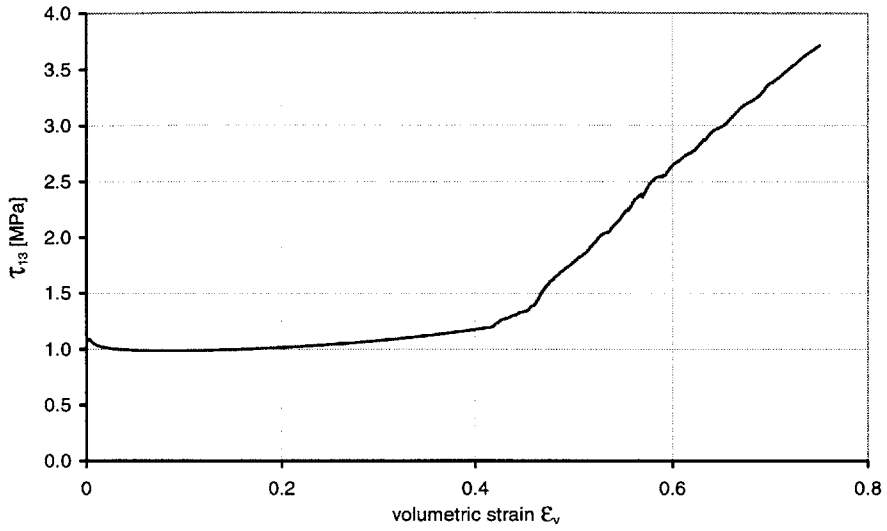

Figure B-4: Macroscopic shear stress γ_{13} as function of the volumetric strain ϵ_v

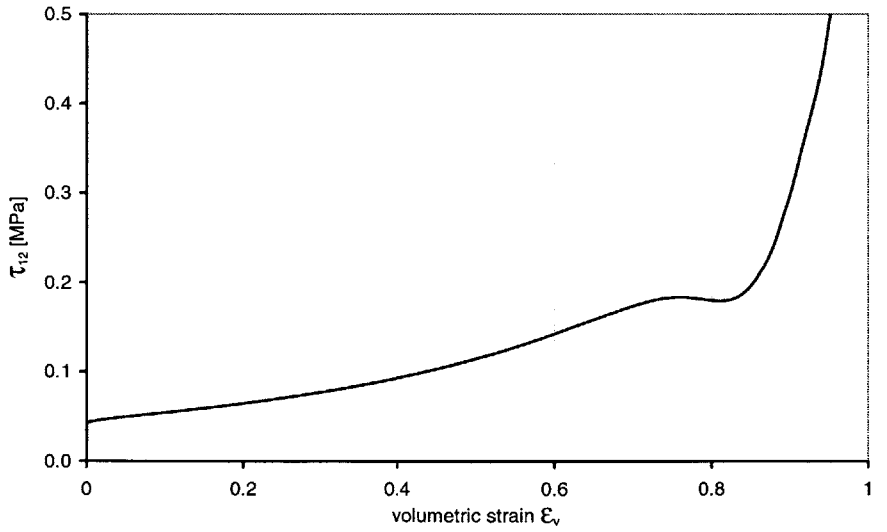

Figure B-5: Macroscopic shear stress γ_{12} as function of the volumetric strain ϵ_v